Prepared for submission to JCAP

Modified propagation of gravitational waves from the early radiation era

Yutong He,[a,b] **Alberto Roper Pol**[c,d,e] **and Axel Brandenburg**[a,b,e,f]

[a]Nordita, KTH Royal Institute of Technology and Stockholm University, Hannes Alfvéns väg 12, SE-10691 Stockholm, Sweden

[b]The Oskar Klein Centre, Department of Astronomy, Stockholm University, AlbaNova, SE-10691 Stockholm, Sweden

[c]Département de Physique Théorique, Université de Genève, CH-1211 Genève, Switzerland

[d]Université Paris Cité, CNRS, Astroparticule et Cosmologie, Paris, F-75013, France

[e]School of Natural Sciences and Medicine, Ilia State University, 3-5 Cholokashvili Ave, Tbilisi, GE-0194, Georgia

[f]McWilliams Center for Cosmology and Department of Physics, Carnegie Mellon University, 5000 Forbes Ave, Pittsburgh, PA 15213, USA

December 13, 2022

E-mail: yutong.he@su.se, alberto.roperpol@unige.ch, brandenb@nordita.org

Abstract. We study the propagation of cosmological gravitational wave (GW) backgrounds from the early radiation era until the present day in modified theories of gravity. Comparing to general relativity (GR), we study the effects that Horndeski parameters, such as the run rate of the effective Planck mass $\alpha_{\rm M}$ and the tensor speed excess $\alpha_{\rm T}$, have on the present-day GW spectrum. We use both the WKB estimate, which provides an analytical description but fails at superhorizon scales, and numerical simulations that allow us to go beyond the WKB approximation. We show that $\alpha_{\rm T}$ makes relatively insignificant changes to the GR solution, especially taking into account the constraints on its value from GW observations by the LIGO-Virgo collaboration, while $\alpha_{\rm M}$ can introduce modifications to the spectral slopes of the GW energy spectrum in the low-frequency regime depending on the considered time evolution of $\alpha_{\rm M}$. The latter effect is additional to the damping or growth occurring equally at all scales that can be predicted by the WKB approximation. In light of the recent observations by pulsar timing array collaborations and future detectors such as SKA, LISA, DECIGO, BBO, or ET, we show that, in most of the cases, constraints can not be placed on the effects of $\alpha_{\rm M}$ and the initial GW energy density $\mathcal{E}^*_{\rm GW}$ separately, but only on the combined effects of the two.

Contents

1 Introduction

The present day Hubble constant, H_0, is measured to be around $H_0 \sim 74\,\mathrm{km/s/Mpc}$ by astrophysical tests using type Ia supernovae [1–3], lensed quasars [4], and megamaser-hosting galaxies [5]. On the other hand, cosmological tests of H_0 constrain its value to $H_0 \sim 67\,\mathrm{km/s/Mpc}$ from cosmic microwave background (CMB) [6] and baryon acoustic oscillations (BAO) [7] experiments, assuming the standard ΛCDM (Λ cold dark matter) model of cosmology. These measurements suggest the presence of a 4–5 σ deviation discrepancy between the early- and late-universe measurements of H_0 [8], known as the Hubble tension. Besides the well-known H_0 tension, a number of other observational discrepancies within the ΛCDM model have been reported, such as the S_8 tension, where $S_8 \propto \sigma_8\,\Omega_{\mathrm{mat},0}^{1/2}$ characterizes the structure growth rate σ_8 and today's matter density $\Omega_{\mathrm{mat},0}$ [9]. A recent summary of over a dozen cosmological tensions and their varied significance can be found in ref. [10].

In view of these tensions, ΛCDM, although being an extremely successful model, does not provide a complete picture and it might be necessary to go beyond it. Since general relativity (GR) is responsible for the gravity sector of ΛCDM, modifying ΛCDM often requires modifying GR. Within the broad subject of modified gravity, Lovelock's theorem proves the uniqueness of GR under four assumptions, and therefore provides four general approaches of modifying GR by relaxing each of them. The theorem states that the only second-order,

local gravitational field equations that can be derived from an action containing only the metric tensor in four dimensions are the Einstein field equations [11, 12]. Therefore, modified theories of gravity could be obtained by: *(i)* adding additional fields other than the metric, *(ii)* constructing theories in a dimension other than four, *(iii)* including higher-than-second-order derivatives, or *(iv)* introducing non-locality; see ref. [13] for a comprehensive review.

Among the plethora of modified gravity mechanisms, we focus on scalar-tensor theories and the phenomenological effects in terms of the modified propagation of gravitational waves (GWs) herein. The choice of scalar-tensor theories is due to their versatility. In other words, apart from extending GR by the inclusion of additional fields, they can also be viewed as the four-dimensional effective description of certain higher-dimensional models after a suitable dimensional reduction, or higher-derivative models after reformulation. Therefore, many modified gravity models following three of the four approaches motivated by circumventing Lovelock's theorem can be comprised into scalar-tensor theories [13]. In addition, generic four-dimensional scalar-tensor models with second-order derivatives can be conveniently summarized in the Horndeski class [14–16]. As a result, Horndeski gravity includes a vast number of different models such as Brans-Dicke [17], quintessence [18], $f(R)$ [19], $f(G)$ [20], k-essence [21], kinetic gravity braiding [22], and galileon [23], among others. Moreover, certain subclass within the Horndeski theories has been shown to ease the Hubble tension [24].

At the level of linear perturbation, Horndeski gravity introduces two parameters to the standard GW equation—the tensor speed excess $\alpha_{\rm T}$ and the running of the effective Planck mass $\alpha_{\rm M}$. The observation of GWs from the binary neutron star merger GW170817 and its multimessenger gamma-ray burst counterpart GRB 170817A [25] has put a tight constraint on the speed of GWs, i.e., $\alpha_{\rm T} \lesssim \mathcal{O}(10^{-15})$, and therefore, on the theory space of Horndeski gravity [26]. However, a large number of models of Horndeski gravity remains viable. Moreover, the constraint only applies to the frequency range that can be probed by LIGO-Virgo and it might not necessarily apply at different frequencies, as proposed in ref. [27]. In fact, this shows the constraining power of GWs as a phenomenological probe. Comparing to $\alpha_{\rm T}$, the constraints on $\alpha_{\rm M}$ are much less stringent [6, 28, 29]. Therefore, in the present work, we focus on exploring $\alpha_{\rm M}$ and its effects on the energy spectrum of GWs. This subclass of Horndeski theories is also known as reduced Horndeski theories. Specifically, we initialize a GW spectrum based on previous studies of GWs sourced by primordial magnetohydrodynamic (MHD) turbulent fields in the early radiation era—e.g., at the electroweak or QCD phase transitions (EWPT or QCDPT)—and then propagate it through cosmic history to obtain the present-day relic spectrum. Actually, we take a generic double broken power law GW spectrum and we show that the obtained results are independent of the initial spectral shape. Hence, our results can be applied to predict the expected GW spectrum from a generic source in Horndeski theories. We then analytically and numerically compare the relic spectra in GR and Horndeski gravity, and discuss their potential observational implications. The numerical solutions in this study are obtained using the Pencil Code [30], which has been used as a tool for simulations of GWs from primordial turbulent sources since the implementation of a GW solver [31]. The cosmological history of the universe is modelled by numerically solving Friedmann equations. We provide a cosmological solver and a tutorial within the associated online material [32]. It also contains the routines that have been used to process the data obtained from the Pencil Code and to generate the results and plots of the present work.

Finally, note that an additional propagating degree of freedom (DOF) appears in Horndeski gravity as a consequence of the scalar field. However, we restrict the current study to

tensor-mode perturbations, since the amplitude of the scalar mode remains subdominant [33], and the discussions of extra DOFs as a smoking gun for modified gravity overall might deserve a separate study.

We introduce the propagation of tensor-mode perturbations described by the GW equation in modified gravity and Friedmann equations in section 2. In section 3, we introduce the WKB approximation, which is commonly used to describe approximate solutions to the GW equation in modified GR. We derive the WKB solution in section 3.1, study its limitations and range of validity in section 3.2, and compute the GW spectrum in section 3.3. Then, in section 4, we present some common parameterizations of the Horndeski parameter $\alpha_{\rm M}$ through the cosmological history of the universe that have been used in the literature, and we present the numerical simulations that we perform to solve the GW equation using the Pencil Code in section 5. We study, in particular, the effects on the GW spectrum that can not be predicted using the WKB approximation. Finally, we discuss potential observational implications of reduced Horndeski theories compared to GR for the different parameterizations of $\alpha_{\rm M}$ in section 6 and conclude in section 7.

Throughout the paper, we set $c = \hbar = k_{\rm B} = 1$, use the metric signature $(-+++)$, and define the gravitational coupling constant $\kappa = 8\pi G_{\rm N}$, where $G_{\rm N}$ is the Newton constant. We indicate with a prime derivatives with respect to conformal time normalized by the conformal Hubble rate at the time of GW generation $\eta\mathcal{H}_*$ and with a dot derivatives with respect to cosmic time t. Both times are related via the scale factor as $a\,{\rm d}\eta = {\rm d}t$.

2 Modified GWs on FLRW background

2.1 GW equation in Horndeski theories

The homogeneous and isotropic background is described by the Friedmann-Lemaître-Robertson-Walker (FLRW) metric. Including tensor perturbations, the FLRW line element reads

$$ {\rm d}s^2 = a^2\big({\rm d}\eta^2 + [\delta_{ij} + a^{-1}h_{ij}(\boldsymbol{x},\eta)]\,{\rm d}x^i\,{\rm d}x^j\big), \tag{2.1} $$

where $h_{ij} = ah_{ij}^{\rm phys}$ are the strains obtained by scaling the physical strains $h_{ij}^{\rm phys}$ with the scale factor a. In GR, the GW equation in Fourier space[1] reads [31, 34]

$$ \tilde{h}_{ij}''(\boldsymbol{k},\eta) + \left(k^2 - \frac{a''}{a}\right)\tilde{h}_{ij}(\boldsymbol{k},\eta) = \frac{6}{a}\tilde{T}_{ij}^{\rm TT}(\boldsymbol{k},\eta), \tag{2.3} $$

where $\mathcal{H} \equiv a'/a$ is the conformal Hubble rate normalized by $\mathcal{H}_*$, and an asterisk refers to a reference time in the early universe, e.g., the time at which the GWs were generated. $\tilde{T}_{ij}^{\rm TT} = \Lambda_{ijlm}\tilde{T}_{lm}$ is the traceless-transverse (TT) projection of the normalized stress energy tensor, i.e., divided by the radiation energy density $\mathcal{E}_{\rm rad} = 3H^2/\kappa$, being $H \equiv \dot{a}/a$ the Hubble rate at time η. The projection operator is $\Lambda_{ijlm}(\hat{\boldsymbol{k}}) = P_{il}P_{jm} - \frac{1}{2}P_{ij}P_{lm}$, where $P_{ij}(\hat{\boldsymbol{k}}) = \delta_{ij} - \hat{k}_i\hat{k}_j$ and $\hat{\boldsymbol{k}} = \boldsymbol{k}/k$. The scale factor at η_* is set to unity, and the wave numbers k are also normalized by the conformal Hubble rate.

[1] We use the Fourier convention

$$ \tilde{h}(\boldsymbol{k}) = \int h(\boldsymbol{x})\,e^{-i\boldsymbol{k}\cdot\boldsymbol{x}}\,{\rm d}^3\boldsymbol{x}, \quad h(\boldsymbol{x}) = \frac{1}{(2\pi)^3}\int \tilde{h}(\boldsymbol{k})\,e^{i\boldsymbol{k}\cdot\boldsymbol{x}}\,{\rm d}^3\boldsymbol{k}. \tag{2.2} $$

In Horndeski gravity [14], the action consists of the metric tensor and an additional scalar field ϕ. Its linear perturbations on the FLRW metric can be characterized by four free parameters separable from the full theory [35]. These free parameters are all arbitrary functions of the scalar field and its kineticity $\nabla_\mu\phi\,\nabla^\mu\phi$. They respectively indicate the following:

- Kineticity $\alpha_{\rm K}$, indicating the kinetic energy of scalar perturbations.
- Braiding $\alpha_{\rm B}$, indicating the mixing of the scalar and tensor kineticities.
- Planck-mass run rate $\alpha_{\rm M}$, denoting the time dependence of the effective Planck mass,

$$\alpha_{\rm M} = \frac{{\rm d}\ln M_{\rm eff}^2}{{\rm d}\ln a}. \tag{2.4}$$

- Tensor speed excess $\alpha_{\rm T}$, measuring the deviation of the speed of gravity from the speed of light.

Out of the four parameters, however, only $\alpha_{\rm M}$ and $\alpha_{\rm T}$ enter and modify the GW equation. As a result, the modifications generalize equation (2.3) to [36]

$$\tilde{h}_{ij}''(\boldsymbol{k},\eta) + \alpha_{\rm M}\mathcal{H}\tilde{h}_{ij}'(\boldsymbol{k},\eta) + \left(c_{\rm T}^2k^2 - \alpha_{\rm M}\mathcal{H}^2 - \frac{a''}{a}\right)\tilde{h}_{ij}(\boldsymbol{k},\eta) = \frac{6}{a}\tilde{T}_{ij}^{\rm TT}(\boldsymbol{k},\eta), \tag{2.5}$$

where $c_{\rm T}$ denotes the GW propagation speed such that $1+\alpha_{\rm T} \equiv c_{\rm T}^2$. The graviton is massless in Horndeski gravity. A massive graviton could be included by adding $m_{\rm g} \neq 0$ in equation (2.5) as done in ref. [37] but we omit it in the present work.

2.2 Friedmann equations

Previous numerical work was usually restricted to specific eras, e.g., radiation (RD) [31, 38–44] or matter domination (MD) [45–47], using a constant equation of state (EOS), defined to be $w \equiv p/\rho$, being p the pressure and ρ the energy density, such that $w = 1/3$ and 0 during RD and MD, respectively. Previous numerical work also ignored the dynamical thermal history of the universe during RD, represented by the relativistic g_* and adiabatic $g_{\rm S}$ DOFs. In GR, the previous formulation is justified since the evolution of the physical strains $h_{ij}^{\rm phys}$ when the source is inactive ($T_{ij} \sim 0$) can be approximated to dilute as $h_{ij}^{\rm phys} \propto a^{-1}$ if one neglects the evolving relativistic DOFs and transitions between radiation, matter, and dark energy dominations (ΛD) [48]. In the present work, we focus on including such effects and solve the GW equation in modified gravity, which present richer dynamics even when the source is inactive, from the time of GW generation up to present time.

However, assuming a piece-wise EOS, such that $w = 1/3$, 0, and -1 during RD, MD, and ΛD, respectively, would create discontinuities in the time evolution of $a(\eta)$ and its derivatives that appear in equation (2.5). Therefore, to find a smooth $a(\eta)$, we directly solve the Friedmann equations,

$$\frac{\ddot{a}}{a} = -\frac{\kappa}{6}\,\rho\big(1+3w\big), \quad \left(\frac{\dot{a}}{a}\right)^2 = \frac{\kappa}{3}\,\rho, \tag{2.6}$$

where the dots denote derivatives with respect to cosmic time t. A more convenient form of equation (2.6) can be expressed in terms of the energy density $\Omega(a)$ and a smooth $w(a)$ as

$$\frac{\ddot{a}}{a} = -\frac{1}{2}H_0^2\,\Omega(a)\big[1+3w(a)\big], \quad \left(\frac{\dot{a}}{a}\right)^2 = H_0^2\,\Omega(a), \tag{2.7}$$

where $\Omega(a)$ is defined to be the ratio of total energy density to the present-day critical energy density $\rho_{\rm crit,0} \equiv 3H_0^2/\kappa$, i.e.,

$$\Omega(a) = \frac{\rho(a)}{\rho_{\rm crit,0}} = \Omega_{\rm rad}(a) + \Omega_{\rm mat}(a) + \Omega_{\Lambda,0} \\ = \left(\frac{a}{a_0}\right)^{-4} \frac{g_*}{g_*^0}\left(\frac{g_{\rm S}}{g_{\rm S}^0}\right)^{-\frac{4}{3}} \Omega_{\rm rad,0} + \left(\frac{a}{a_0}\right)^{-3} \Omega_{\rm mat,0} + \Omega_{\Lambda,0}. \tag{2.8}$$

Numerically, we take the present-time values of $\Omega_{\Lambda,0} \simeq 0.684$, $\Omega_{\rm rad,0} \simeq 4.16 \times 10^{-5}\, h^{-2}$, and $\Omega_{\rm mat,0} = 1 - \Omega_{\rm rad,0} - \Omega_{\Lambda,0} \simeq 0.316$, where h takes into account the uncertainties on the present-time Hubble rate $H_0 = 100\, h$ km/s/Mpc. We set $h \simeq 0.67$ for the numerical studies, using the value observed from the CMB, and $g_*^0 \simeq 3.36$ and $g_{\rm S}^0 \simeq 3.91$ are the reference relativistic and adiabatic DOFs at the present time[2].

The evolution of the relativistic and adiabatic DOFs as a function of the temperature during RD are taken from ref. [49] and expressed as a function of a by taking $a^3\, T^3 g_{\rm S}$ to be constant, following an adiabatic expansion of the universe.

The characteristic EOS, corresponding to the energy density of equation (2.8), can be computed combining equations (2.7) by taking the time derivative of the second equation and introducing the first equation. This yields

$$\frac{\dot{\Omega}(a)}{\Omega(a)} = -3(1+w)\frac{\dot{a}}{a}, \tag{2.10}$$

which allows us to compute $w(a)$ using equation (2.8),

$$w(a) = \left(\frac{1}{3}\Omega_{\rm rad}(a) - \Omega_{\Lambda,0}\right)\Omega^{-1}(a). \tag{2.11}$$

Equation (2.10) justifies the expected evolution of $\Omega(a)$ used in equation (2.8): approximately proportional to a^{-4} during the RD era, to a^{-3} during the MD era, and constant during ΛD. During RD, the evolution of DOFs induces some modifications with respect to the a^{-4} evolution. Equation (2.11) yields $w = 1/3$ for RD, $w = 0$ for MD, and $w = -1$ for ΛD, as expected. In the intermediate times, the functions $\Omega(a)$ and $w(a)$ transition smoothly. With equations (2.8) and (2.11) explicitly in terms of a, we can compute the relevant quantities that appear in the modified GW equation (2.5), given in equation (2.7), and expressed in terms of the normalized conformal time $\eta\mathcal{H}_*$ as

$$\mathcal{H} = \frac{H_0}{\mathcal{H}_*}\, a\sqrt{\Omega(a)}, \quad \frac{a''}{a} = \frac{1}{2}\mathcal{H}^2\big[1 - 3w(a)\big], \tag{2.12}$$

where the term $\mathcal{H}_*$ appears due to our definition of the normalized $\mathcal{H} = a'/a$, and we set $a_* = 1$ for consistency with our GW equation; see discussion below equation (2.3). Finally,

[2]Note that neutrinos' contribution to the radiation energy density is accounted for by taking

$$g_*^0 = 2\left[1 + N_{\rm eff}\frac{7}{8}\left(\frac{4}{11}\right)^{\frac{4}{3}}\right] \simeq 3.363, \tag{2.9}$$

where $N_{\rm eff} \approx 3$, instead of $g_*^0 = 2$ at the present day due to photons only. This leads to an excess in the calculation of the radiation energy density after neutrinos become massive. However, this occurs when the radiation energy is subdominant and hence, it does not affect our calculations.

since equation (2.5) is expressed in terms of conformal time η but equation (2.12) is still written in terms of a, we would like to substitute the variables via $a(t)$ or $a(\eta)$, which can be obtained using equation (2.7):

$$\dot{a} = H_0\, a\sqrt{\Omega(a)} \Rightarrow \mathrm{d}\big(H_0 t\big) = \frac{\mathrm{d}a}{a\sqrt{\Omega(a)}} \Rightarrow H_0\big(t - t_{\rm ini}\big) = \int_{a_{\rm ini}}^{a} \frac{\mathrm{d}a}{a\sqrt{\Omega(a)}}. \tag{2.13}$$

This allows us to compute $t(a)$ and then invert the relation to obtain $a(t)$. Similarly, in conformal time we have $\mathrm{d}t = a\,\mathrm{d}\eta$, so we solve

$$H_0\big(\eta - \eta_{\rm ini}\big) = \int_{a_{\rm ini}}^{a} \frac{\mathrm{d}a}{a^2\sqrt{\Omega(a)}}. \tag{2.14}$$

For the numerical integration, we set $a_{\rm ini} = 10^{-20}$ at $t_{\rm ini} = \eta_{\rm ini} = 0$, which yields accurate results for all $a \gtrsim 10^{-19}$. Further details and numerical results to this equation can be found on the `GW_turbulence` GitHub project [32].

In the present work, we consider that the GWs are generated during a phase transition (in particular, at the EWPT or QCDPT) within the RD era. Assuming adiabatic expansion of the universe, one can compute a_*/a_0 as a function of the temperature T_* and the adiabatic DOFs,

$$\frac{a_*}{a_0} = \frac{T_0}{T_*}\left(\frac{g_{\rm S}^0}{g_{\rm S}}\right)^{\frac{1}{3}} \simeq 7.97\times10^{-16}\,\frac{T_*}{100\ \mathrm{GeV}}\left(\frac{g_{\rm S}}{100}\right)^{-\frac{1}{3}}, \tag{2.15}$$

where we take $T_0 \simeq 2.7255\,\mathrm{K}$. Setting $a_* = 1$, such that $\mathcal{H}_* = H_*$, this gives a value of the Hubble rate (valid during the RD era),

$$\mathcal{H}_* = \frac{\pi T_*^2}{3}\sqrt{\frac{\kappa\, g_*}{10}} \simeq 2.066\times10^{10}\,\mathrm{Hz}\left(\frac{T_*}{100\,\mathrm{GeV}}\right)^2\left(\frac{g_*}{100}\right)^{\frac{1}{2}}, \tag{2.16}$$

with[3] $\eta_* \approx \mathcal{H}_*^{-1}$. These results allow us to use the solutions from Friedmann equations and adapt them to compute the variables that appear in equation (2.5), normalized to the specific epoch of GW generation.

3 WKB approximation

3.1 Solution of the GW equation

Modifications of the GW propagation, in the absence of sources[4] (i.e., $T_{ij} = 0$), have been studied using the WKB approximation [29, 50]. The WKB solution can be obtained using the following ansatz

$$\tilde{h}_{ij}(k,\eta) = h(k,\eta)\, e_{ij} = A e_{ij}\, e^{iB}, \tag{3.1}$$

[3] During RD with $w = \frac{1}{3}$, $\eta = 1/\mathcal{H}$ holds exactly, but the dependence of the radiation energy density with g_* and $g_{\rm S}$ induce small deviations.

[4] In the absence of sources, the GW equation [see equation (2.5)] does not depend on the wave vector $\boldsymbol{k}$ but only on its modulus (the wave number) k. Hence, the solution can simply be expressed as a function of k.

where A and B are generic coefficients, and e_{ij} is the polarization tensor.[5] Substituting this into equation (2.5), one gets

$$2\frac{A'}{A} + \frac{B''}{B'} + \alpha_{\rm M}\mathcal{H} = 0 \Rightarrow A(\eta) = e^{-\mathcal{D}}, \tag{3.2}$$

$$B'^2 = \frac{A''}{A} + \alpha_{\rm M}\mathcal{H}\frac{A'}{A} + k^2c_{\rm T}^2 - \alpha_{\rm M}\mathcal{H}^2 - \frac{a''}{a} \approx k^2c_{\rm T}^2 \Rightarrow B(k,\eta) = \pm k(\eta\mathcal{H}_* - \Delta T), \tag{3.3}$$

where, following the WKB approximation, we neglect the terms A''/A, A'/A, $\mathcal{H}^2$, and a''/a, when compared to $k^2c_{\rm T}^2$. In addition, we also neglect the term $B''/B' \sim c_{\rm T}'/c_{\rm T} \sim 0$. We have defined the damping factor $\mathcal{D}$ and the time delay due to the effective GW speed ΔT that appear in modified theories of gravity [50]

$$\mathcal{D}(\eta) = \frac{1}{2}\int_1^{\eta\mathcal{H}_*} \alpha_{\rm M}\mathcal{H}\,{\rm d}\eta', \quad \Delta T(\eta) = \int_1^{\eta\mathcal{H}_*} (1 - c_{\rm T})\,{\rm d}\eta'. \tag{3.4}$$

Hence, the solution is

$$h(k,\eta) = e^{-\mathcal{D}}e^{\pm ik(\eta\mathcal{H}_* - \Delta T)} = e^{-\mathcal{D}\mp ik\Delta T}h^{\rm GR}(k,\eta), \tag{3.5}$$

where $\mathcal{D} = \Delta T = 0$ in GR. For the initial conditions[6] $h(k,\eta_*) = h_*(k)$ and $h'(k,\eta_*) = h'_*(k)$, we get

$$\begin{aligned} h(k,\eta) &= e^{-\mathcal{D}}\left[h_*(k)\cos k(\eta\mathcal{H}_* - 1 - \Delta T) + \frac{h'_*(k) + \frac{1}{2}\alpha_{\rm M}^* h_*(k)}{kc_{\rm T}}\sin k(\eta\mathcal{H}_* - 1 - \Delta T)\right], \\ &= e^{-\mathcal{D}}\left[h_*(k)\cos k\,\tilde{c}_{\rm T}(\eta\mathcal{H}_* - 1) + \frac{h'_*(k) + \frac{1}{2}\alpha_{\rm M}^* h_*(k)}{kc_{\rm T}}\sin k\,\tilde{c}_{\rm T}(\eta\mathcal{H}_* - 1)\right], \end{aligned} \tag{3.6}$$

where $\alpha_{\rm M}^* = \alpha_{\rm M}(\eta_*)$ and $\tilde{c}_{\rm T}(\eta) = \int c_{\rm T}\,{\rm d}\eta'/(\eta\mathcal{H}_* - 1)$. Note that the specific choice of initial conditions does not allow to give a linear relation between h and $h^{\rm GR}$ as done in ref. [50] and, in general, $h \neq e^{-\mathcal{D}-ik\Delta T}h^{\rm GR}$, which is only true when referring to the particular solution of the ODE, given in equation (3.5). This reduces to the solution in GR when $c_{\rm T} = \tilde{c}_{\rm T} = 1$ and $\alpha_{\rm M} = 0$,

$$h^{\rm GR}(k,\eta) = h_*(k)\cos k(\eta\mathcal{H}_* - 1) + \frac{h'_*(k)}{k}\sin k(\eta\mathcal{H}_* - 1). \tag{3.7}$$

In reduced Horndeski theories with $\alpha_{\rm T} = 0$, the WKB solution yields

$$h(k,\eta) = e^{-\mathcal{D}}\left[h^{\rm GR}(k,\eta) + \tfrac{1}{2}\alpha_{\rm M}^*\frac{h_*(k)}{k}\sin k(\eta\mathcal{H}_* - 1)\right]. \tag{3.8}$$

When $\alpha_{\rm M} = 0$ and $c_{\rm T}$ is a constant in time we find

$$h(k,\eta) = h_*(k)\cos\big[kc_{\rm T}(\eta\mathcal{H}_* - 1)\big] + \frac{h'_*(k)}{kc_{\rm T}}\sin\big[kc_{\rm T}(\eta\mathcal{H}_* - 1)\big]. \tag{3.9}$$

[5] In the absence of sources, the GW propagation of any polarization mode is the same, so we can just call h the amplitude of each mode. If the produced GW signal is polarized, then for each mode we need to impose the corresponding initial conditions.

[6] In the current work, we focus on the propagation of a GW background after it has already been generated and reached a stationary solution, when the source is no longer active. Since the propagation only depends on k, the initial conditions can be computed from the 3D fields in Fourier space, after shell integration over directions $\hat{\boldsymbol{k}}$, for each polarization mode.

3.2 Limitations of the WKB approximation

To obtain the WKB solution we have neglected some terms in equation (3.3) that would otherwise appear in the solution. These terms can be expressed in the following way

$$\frac{A''}{A}+\alpha_{\rm M}\mathcal{H}\frac{A'}{A}-\alpha_{\rm M}\mathcal{H}^2-\frac{a''}{a}=-\tfrac{1}{2}\alpha_{\rm M}\Big(1+\tfrac{1}{2}\alpha_{\rm M}\Big)\mathcal{H}^2-\tfrac{1}{2}\alpha'_{\rm M}\mathcal{H}-\frac{a''}{a}\Big(1+\tfrac{1}{2}\alpha_{\rm M}\Big), \tag{3.10}$$

where we have used $\mathcal{H}'=a''/a-\mathcal{H}^2$. Hence, the WKB assumption could break down when at least one of these terms is not negligible when compared to $k^2c_{\rm T}^2$. We have one term that depends on $\alpha_{\rm M}$, one term that depends on the time evolution of $\alpha_{\rm M}$, and one term that depends on a''/a. The latter appears also in GR when WKB is used to approximate the solution for the scaled strains, which do not decay (note that the decay of the physical strains is already absorbed by the scale factor), as shown in equation (3.7). This term is given in equation (2.12) and its upper bound can be found using Friedmann equations

$$\frac{a''}{a}\leq\frac{1}{2}\frac{\Omega_{\rm mat,0}}{\Omega_{\rm rad,0}}\frac{g_*}{g_*^0}\left(\frac{g_{\rm S}}{g_{\rm S}^0}\right)^{-\frac{4}{3}}\mathcal{H}\,\frac{a_*}{a_0}\lesssim 10^4\,h^2\,\mathcal{H}\,\frac{a_*}{a_0}, \tag{3.11}$$

where the first inequality is an approximation valid during the RD era and it decays during MD. Hence, the upper bound is valid at all times and its specific value depends on a_*/a_0. For example, for GWs generated at the EWPT or at the QCDPT, this leads to the following limiting wave numbers (for $h=0.67$), at which the WKB approximation might break down,

$$k^{\rm EW}_{{\rm lim},\,a''}\sim 1.87\times10^{-6}\,\mathcal{H}\sqrt{\frac{\left|1+\frac{1}{2}\alpha_{\rm M}\right|}{c_{\rm T}}}\leq 1.87\times10^{-6}\sqrt{\frac{\left|1+\frac{1}{2}\alpha_{\rm M}\right|}{c_{\rm T}}}, \tag{3.12}$$

$$k^{\rm QCD}_{{\rm lim},\,a''}\sim 5.90\times10^{-5}\,\mathcal{H}\sqrt{\frac{\left|1+\frac{1}{2}\alpha_{\rm M}\right|}{c_{\rm T}}}\leq 5.90\times10^{-5}\sqrt{\frac{\left|1+\frac{1}{2}\alpha_{\rm M}\right|}{c_{\rm T}}}. \tag{3.13}$$

In both cases, this term is subdominant up to very large superhorizon scales and it is bounded by the values in equations (3.12) and (3.13) since $\mathcal{H}=\eta_*/\eta$ during RD era as can be seen using equation (2.12). This limit can be modified by the inclusion of $\alpha_{\rm M}$ and $\alpha_{\rm T}$ but unless they take large values these modifications are negligible.

On the other hand, two additional limitations to the WKB approximation appear due to the $\alpha_{\rm M}$ parameter,

$$k_{{\rm lim},\,\alpha_{\rm M}}\sim\frac{\mathcal{H}}{c_{\rm T}}\sqrt{\left|\frac{\alpha_{\rm M}}{2}\Big(1+\tfrac{1}{2}\alpha_{\rm M}\Big)\right|}\lesssim\frac{1}{c_{\rm T}}\sqrt{\frac{|\alpha_{\rm M}^*|}{2}},\quad k_{{\rm lim},\,\alpha'_{\rm M}}\sim\frac{\mathcal{H}}{c_{\rm T}}\sqrt{\frac{|\alpha'_{\rm M}|}{2}}\leq\frac{1}{c_{\rm T}}\sqrt{\frac{|\alpha'^*_{\rm M}|}{2}}, \tag{3.14}$$

where we can neglect the term $\frac{1}{2}\alpha_{\rm M}$ in front of 1 in the first limit for small values of $\alpha_{\rm M}$. Hence, the WKB limit can break down in Horndeski theories around the horizon or at larger scales. In general, we expect the limit from $\alpha_{\rm M}$ to be more restrictive than that from $\alpha'_{\rm M}$ and to dominate at the initial time when $\mathcal{H}=1$. However, this depends on the parameterization of $\alpha_{\rm M}$, which can give different results for both limits; see section 4.

3.3 GW spectrum using the WKB approximation

The spectrum of GW energy density can be expressed as

$$\Omega_{\rm GW}(k,\eta)=\frac{1}{\rho_{\rm crit,0}}\frac{{\rm d}\ln\rho_{\rm GW}}{{\rm d}\ln k}=\frac{1}{6}\left(\frac{H_*}{H_0}\right)^2\left(\frac{a_*}{a_0}\right)^4 kS_{h'}(k,\eta), \tag{3.15}$$

where $2S_{h'}$ is the spectrum[7] of the scaled strain derivatives,

$$\langle \tilde{h}'_{ij}(\boldsymbol{k},\eta)\, \tilde{h}'^{*}_{ij}(\boldsymbol{k}',\eta)\rangle = (2\pi)^6 \delta^3(\boldsymbol{k}-\boldsymbol{k}')\frac{2S_{h'}(k,\eta)}{4\pi k^2}, \tag{3.17}$$

and it can be computed using the WKB approximation. Taking $\mathcal{D}' = \frac{1}{2}\alpha_{\rm M}\mathcal{H}$, the modified GW energy spectrum can be obtained using the WKB solution for Horndeski theories, given in equation (3.6), and assuming that at times $\eta \geq \eta_*$ the GWs are in the free-propagation regime, such that $|h'(k,\eta)| = k\,|h(k,\eta)|$,

$$\Omega_{\rm GW}\,(k,\eta) = e^{-2\mathcal{D}}\Omega^{\rm GR}_{\rm GW}(k,\eta)\,\xi(k,\eta), \tag{3.18}$$

where $\xi(k,\eta)$ corresponds to the spectral modifications with respect to the GR spectrum after taking into account the amplification (or depletion) produced by the damping factor $\mathcal{D}$,

$$\xi(k,\eta) = 1 + \tfrac{1}{2}\alpha_{\rm T} + \frac{{\alpha^*_{\rm M}}^2\alpha^2_{\rm M}\mathcal{H}^2}{32k^4c^2_{\rm T}} + \frac{\alpha^*_{\rm M}\alpha^2_{\rm M}\mathcal{H}^2}{8k^3c^2_{\rm T}} + \frac{1}{8k^2}\left[\alpha^2_{\rm M}\mathcal{H}^2\left(1+\frac{1}{c^2_{\rm T}}\right) + {\alpha^*_{\rm M}}^2\right] + \frac{\alpha^*_{\rm M}}{2k}. \tag{3.19}$$

We have further averaged over oscillations in time η, such that the expression is valid at $k\,\tilde{c}_{\rm T} \gtrsim (\eta\mathcal{H}_* - 1)^{-1}$. At late times, $\mathcal{H}^2 = (\eta_*/\eta)^2$ becomes small, so we can neglect the terms that dilute with $\mathcal{H}^2$,

$$\xi(k,\eta \gg \eta_*) = \tfrac{1}{2}\big(1+\alpha_{\rm T}\big) + \tfrac{1}{2}\Big(1+\frac{\alpha^*_{\rm M}}{2k}\Big)^2. \tag{3.20}$$

From equation (3.20), we can identify the IR and UV limiting ranges of the spectrum,

$$\Omega^{\rm IR}_{\rm GW} = \Omega_{\rm GW}\Big(k \ll \tfrac{1}{2}\alpha^*_{\rm M}, \eta \gg \eta_*\Big) = \frac{{\alpha^*_{\rm M}}^2}{8k^2}\, e^{-2\mathcal{D}}\,\Omega^{\rm GR}_{\rm GW}(k,\eta), \tag{3.21}$$

$$\Omega^{\rm UV}_{\rm GW} = \Omega_{\rm GW}\Big(k \gg \tfrac{1}{2}\alpha^*_{\rm M}, \eta \gg \eta_*\Big) = \Big(1+\tfrac{1}{2}\alpha_{\rm T}\Big)\, e^{-2\mathcal{D}}\,\Omega^{\rm GR}_{\rm GW}(k,\eta). \tag{3.22}$$

Note that the factor ${\alpha^*_{\rm M}}^2$ is part of the IR limit, indicating that the IR enhancement of the form k^{-2} holds regardless of the sign of $\alpha^*_{\rm M}$. The critical $k_{\rm crit} = \frac{1}{2}|\alpha^*_{\rm M}|$ indicates where the IR regime begins, i.e., the k^{-2} term in equation (3.20) becomes dominant.

Equation (3.20) shows that the GW spectrum in the IR regime can present up to k^{-4} modifications to the GR spectrum but this and other terms vanish as time evolves since they are proportional to $\mathcal{H}^2$. Hence, at late times, we end up with the GR spectrum amplified (or diluted for positive $\mathcal{D}$) by $e^{-2\mathcal{D}}$ at all wave numbers with a k^{-2} enhancement in the IR regime, proportional to the additional $\frac{1}{8}{\alpha^*_{\rm M}}^2$ factor, as shown in equation (3.21). In the UV regime, we find the $e^{-2\mathcal{D}}$ enhancement (or depletion) and an additional factor $1+\frac{1}{2}\alpha_{\rm T}$. The sign of $\alpha_{\rm T}$ determines if the GW spectrum is amplified or decreased with respect to that obtained from GR.

We have found that, according to the WKB approximation, the parameter $\alpha_{\rm M}$ introduces changes in the spectral shape at $k \leq k_{\rm crit} = \frac{1}{2}|\alpha^*_{\rm M}|$ that do not dilute as time evolves and depend on the value of $\alpha_{\rm M}$ only at the time of GW generation. On the other hand, note

[7] Following ref. [31], we define the spectrum $S_{h'}(k,\eta)$ from the + and × polarization modes, giving an extra factor of 2 due to the property

$$\tilde{h}'_{ij}(\boldsymbol{k},\eta)\,\tilde{h}'^{*}_{ij}(\boldsymbol{k}',\eta) = 2\big[h'_{+}(\boldsymbol{k},\eta)\,h'^{*}_{+}(\boldsymbol{k}',\eta) + h'_{\times}(\boldsymbol{k},\eta)\,h'^{*}_{\times}(\boldsymbol{k}',\eta)\big]. \tag{3.16}$$

that, using equation (3.14), we can estimate the WKB approximation to break down around $k \sim \max(k_{\mathrm{lim},\,\alpha_{\mathrm{M}}}, k_{\mathrm{lim},\,\alpha'_{\mathrm{M}}})$. This means that when $\mathcal{H} \sim 1$, the spectral changes occur at wave numbers around and below the critical k_{crit}, where the WKB approximation might not be valid (for $c_{\mathrm{T}} \sim 1$).

We investigate the resulting spectra in modified GR using numerical simulations in section 5 with the objective to test the validity of the WKB approximation and its potential limitations and to confirm the resulting GW spectra when Horndeski parameters are introduced due to modified theories of gravity.

4 Phenomenological parameterizations

In section 3.3, we noted that, according to the WKB approximation, $\alpha_{\mathrm{T}} \neq 0$ induces modifications in the total GW energy density, but not in its spectral shape. Realistically, the tensor speed excess at the present day is observationally constrained to be $\alpha_{\mathrm{T},0} \lesssim \mathcal{O}(10^{-15})$ by the binary neutron star merger GW170817 and its gamma-ray burst GRB 170817A [25]. This constraint can be circumvented if α_{T} is either frequency- or time-dependent, such that larger deviations could hide outside the LIGO-Virgo frequency band [51, 52] or in the past. In this study, we show that even using larger values of α_{T}, constant in time and frequency, the modifications to the GW spectrum are negligible, which is seen from the WKB approximation and can be confirmed with numerical simulations. Hence, from now on, we will focus on two cases: *(i)* constant α_{T} with $\alpha_{\mathrm{M}} = 0$, and *(ii)* reduced Horndeski theories with $\alpha_{\mathrm{T}} = 0$, allowing α_{M} to take different values as a function of time.

In particular, we are interested in the perspectives of negative values of α_{M}, as they would enhance the amplitude of the GW spectrum. Various constraints on the present-day value $\alpha_{\mathrm{M},0}$ exist in the literature, but are significantly less stringent than those on α_{T}. Assuming the cosmic acceleration due to scalar-tensor theories of gravity, it can be shown that $|\alpha_{\mathrm{M}}| \lesssim 0.5$ at late times (see figure 4 in ref. [28]). This is compatible with the numerical results of ref. [29] (see their figure 2), giving $|\alpha_{\mathrm{M},0}| \lesssim 1$. On the other hand, the Planck Collaboration reports a slightly tighter constraint on $\alpha_{\mathrm{M},0} \gtrsim -0.1$ (see table 8 of ref. [6]). Note that they parameterize $\alpha_{\mathrm{M}} = \alpha_{\mathrm{M},0}\,(a/a_0)^n$ with $n \in (0.5, 1)$. Taking these different constraints into account, we explore a range of $\alpha_{\mathrm{M},0} \in [-0.5, 0.3]$.

Besides the simplest consideration of a constant α_{M} in time, which we call choice 0, its time-dependent forms can be written in accordance with specific gravity models [53]. Following refs. [35, 36, 54], we choose phenomenological forms of α_{M} as simplified parameterizations motivated by effective descriptions of modified gravity [55]. Specifically:

$$\alpha_{\mathrm{M}}(\eta) = \begin{cases} \alpha_{\mathrm{M},0} & \text{(choice 0)}, \\ \alpha_{\mathrm{M},0} \left[\dfrac{a(\eta)}{a_0}\right]^n & \text{(choice I)}, \\ \alpha_{\mathrm{M},0} \dfrac{1}{\Omega(\eta)} & \text{(choice II)}, \\ \alpha_{\mathrm{M},0} \dfrac{1 - \Omega_{\mathrm{mat}}(\eta)/\Omega(\eta)}{1 - \Omega_{\mathrm{mat},0}} & \text{(choice III)}, \end{cases} \tag{4.1}$$

where choices II and III give a value of α_{M} proportional to the percentage of dark energy density and the combination of dark and radiation energy densities, respectively, at each time η compared to their relative amounts at the present time. For choice I, the following

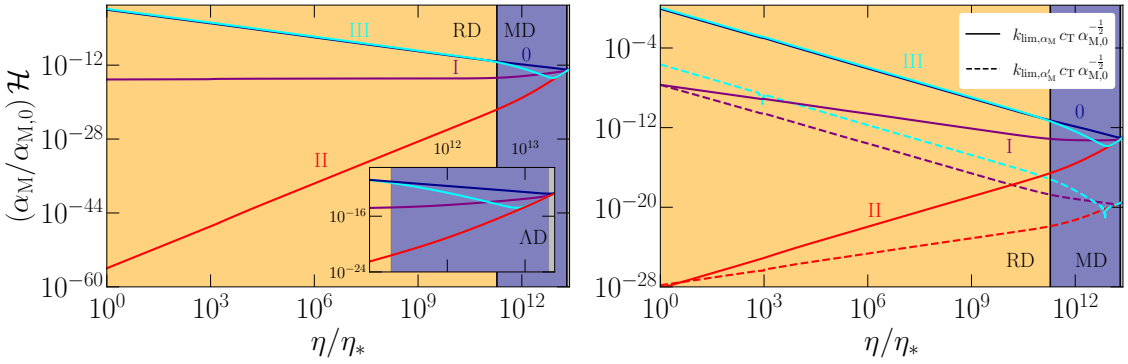

Figure 1: Time evolution of $\alpha_M\mathcal{H}$ (left panel), which contributes to the change of amplitude over time, $h_{ij} \sim e^{-\mathcal{D}}$ with $\mathcal{D} = \frac{1}{2}\int^\eta \alpha_M\mathcal{H}\,d\eta'$, and $k_{\mathrm{lim},\,\alpha_M}\,c_T$ and $k_{\mathrm{lim},\,\alpha'_M}\,c_T$ (right panel) are the terms neglected when compared to kc_T under the WKB approximation; see equation (3.14). All four parameterization choices (0 to III) are shown and, for illustrative purposes, $n = 1$ is chosen. The main figures show the full evolution whereas the inset (in left panel) shows only times after the onset of MD. We have taken η_* to correspond to the EWPT for the specific values in the axes, which puts the present time at $\eta_0/\eta_* \simeq 2.4\times10^{13}$.

conditions on the parameter values are needed in order to ensure the theory's stability [56]:

$$\text{stability for: } \begin{cases} 0 < n < \frac{3}{2}\,\Omega_{\mathrm{mat},0} \simeq \frac{1}{2}, & \text{if } \alpha_{M,0} > 0, \\ n > \frac{3}{2}, & \text{if } \alpha_{M,0} < 0. \end{cases} \tag{4.2}$$

To provide an intuition on the aforementioned α_M parameterizations, we show in figure 1 (left panel), for the different time dependencies given in equation (4.1), the evolution of $\alpha_M\mathcal{H}$, which characterizes the growth or damping produced by α_M, according to the WKB approximation [see equation (3.4)]. We also show the time evolutions of $k_{\mathrm{lim},\,\alpha_M}\,c_T$ and $k_{\mathrm{lim},\,\alpha'_M}\,c_T$ (right panel), which correspond to the wave numbers at which the WKB approximation might break down, according to equation (3.14). Figure 1 shows the time evolution from the time of generation (e.g., EWPT) up to present time. We see that for choices 0 and III, $\alpha_M\mathcal{H}$ converges to the same values during RD and ΛD, and only becomes different during MD, as expected. On the other hand, for choices I and II, $\alpha_M\mathcal{H}$ is negligible for all of RD and most of MD and rapidly increases later on, especially during ΛD. It converges for all parameterizations to the value $\alpha_{M,0}$ at the present time.

We see in figure 1 (right panel) that for choices 0 and III, the limiting k is around the horizon scale at the time of generation, i.e., $k_{\mathrm{lim},\,\alpha_M}\,c_T \sim \sqrt{\alpha_M^*/2}$ and then it decreases into superhorizon scales since it is proportional to $\mathcal{H} = \eta_*/\eta$ (this is because for these choices, $\alpha_M \simeq \alpha_M^*$ during the RD era). The term $\alpha'_M = 0$ for choice 0 and $\alpha'_M \ll \alpha_M$ for choice III, as can be seen in figure 1. The ratio between α_M and α'_M during the RD era can be found to be

$$\left(\frac{\alpha_M}{\alpha'_M}\right)^{\frac{1}{2}}_{\mathrm{III}} \sim 10^2\left(\frac{a_*}{a_0}\right)^{\frac{1}{2}} \simeq 3\times10^{-6}\left(\frac{a_*}{8\times10^{-16}}\right)^{\frac{1}{2}}, \tag{4.3}$$

which only becomes of order 1 when the time of GW generation is around the end of the RD era, i.e., $a_*/a_0 \sim 10^{-4}$, which corresponds to times much later than the EWPT and the QCDPT. For choices I and II, although the two terms are of the same order, $\alpha'^*_M \sim \alpha^*_M$, their

value at the time of GW generation is much smaller than $\alpha_{\rm M,0}$ (for all $n > 0$ in the choice I). For this reason, in these cases the WKB estimate is completely valid and we do not expect to observe any relevant spectral change, since the IR enhancement is determined by the value of $\alpha_{\rm M}^*$, as seen in equation (3.20).

Note that, since many efforts of modifying gravity are aimed at addressing the late-time acceleration of the universe, the $\alpha_{\rm M}$ parameterization choices are commonly constructed to be dominant in the late universe. This is indeed the case for choices I and II here. If one considers only the MD and ΛD history of the universe, choice III is also well-motivated to be relevant at late times. However, here we explore the entire history of the universe from well within RD, which means that $\alpha_{\rm M}\mathcal{H}$ becomes dominant for choice III both at early and late times. We note that the physical motivations of the choices here can be potentially ambiguous. Even though there exists a wide range of discussions on modified gravity during inflation [36, 57] and around recombination [58, 59], where $\alpha_{\rm M}$ is essentially a free function of the scalar field, there seems to be a relative lack of numerical studies on the effects of $\alpha_{\rm M}$ during RD (note, however, a brief discussion of $\alpha_{\rm M} = -1$ during RD in ref. [60]). Hence, we emphasize that the aim of this work is to provide an understanding of the phenomenological behavior of the GW spectrum due to $\alpha_{\rm M}$ for signals produced during RD.

5 Numerical solutions

To explore the limits and validity of the WKB approximation, we use the Pencil Code to numerically solve the GW equation under modified gravity, given in equation (2.5). The Pencil Code is a highly parallelized modular code that can be used to solve various differential equations [30]. In the context of cosmological GWs, it has previously been used to study GWs generated by hydrodynamic and MHD stresses in the early universe [38]. It uses a GW solver that advances the strains at each time step sourced by the anisotropic stresses that are separately computed as the solution to the MHD equations [31]. Previous numerical works solved the GW equation under GR, while in the present work, we have extended the code to solve equation (2.5); see appendix A for further details on the numerical scheme.

5.1 Initial condition and time stepping schemes

In the current work, we focus primarily on the propagation rather than the production of GWs. Therefore, we have adapted the Pencil Code to evolve an initial GW spectrum in the absence of sources with a spectral shape and amplitude based on those obtained in previous studies (see, e.g., refs. [37, 43]). Hence, equation (2.5) is solved in one-dimension (i.e., in $k > 0$) in order to improve the efficiency of the code when studying the propagation of a GW background along the cosmological history of the universe. We take the initial spectrum for the time derivative of the strains, defined in equation (3.17), to be a smoothed double broken power law described by

$$S_{h'}(k,\eta_*) = S_{h'}^* \frac{2^{\frac{1}{\alpha_2}}\left[1+\left(\frac{k_*}{k_{\rm b}}\right)^{a-b}\right]\left(\frac{k}{k_*}\right)^a}{\left[1+\left(\frac{k}{k_{\rm b}}\right)^{(a-b)\alpha_1}\right]^{\frac{1}{\alpha_1}}\left[1+\left(\frac{k}{k_*}\right)^{(b+c)\alpha_2}\right]^{\frac{1}{\alpha_2}}}, \tag{5.1}$$

where $S_{h'}^*$ is approximately the initial peak amplitude, $\eta_* \approx \mathcal{H}_*^{-1}$ corresponds to the time of GW production during the RD era, and $\alpha_1 = \alpha_2 = 2$ are fixed smoothness parameters. We

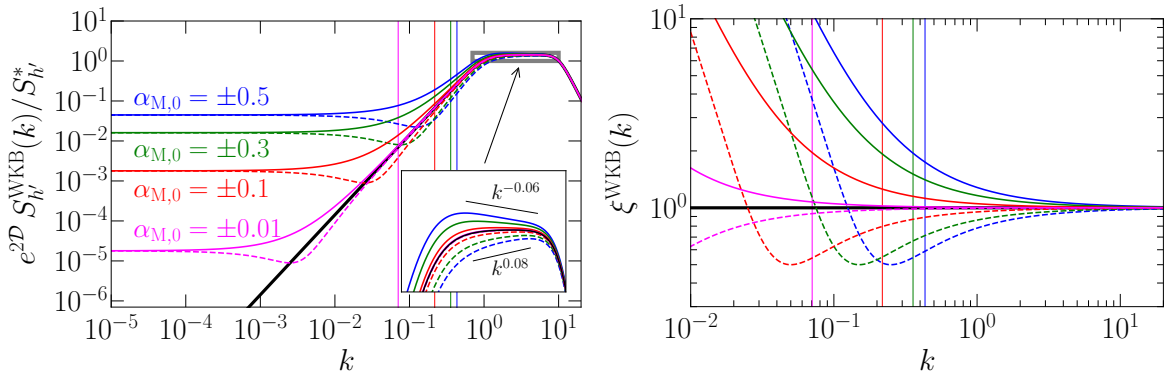

Figure 2: *Left panel:* Expected WKB spectra [see equation (3.18)] of the strain derivatives $S_{h'}(k)$, compensated by $e^{-2\mathcal{D}}$, at late times due to non-zero $\alpha_{\rm M}^{*}$ at the time of generation for an initial GW background characterized by a double broken power law, given in equation (5.1). *Right panel:* Expected spectral modifications $\xi^{\rm WKB}(k) \equiv e^{2\mathcal{D}} S_{h'}^{\rm WKB}(k)/S_{h'}^{\rm GR}(k)$, given in equation (3.20). The black curves indicate the GR solution and the colored curves correspond to different values of $\alpha_{\rm M}^{*}$, with the solid and dashed ones being positive and negative values, respectively. Vertical lines indicate the estimated value of $k_{\rm lim,\,\alpha_M}$, below which the WKB approximation might fail. The inset zooms in on the behaviors around the horizon at $k \in (1, 10)$.

similarly initialize the spectrum of the strains $S_h(k, \eta_*) = S_{h'}(k, \eta_*)/k^2$. We choose the slope in the IR range to be k^2, set by $a = 2$ (as is expected for causal sources of GWs, as those produced for example during a phase transition) up to the break wave number $k_{\rm b} = 1$, which corresponds to the horizon scale. At intermediate wave numbers, $k_{\rm b} \leq k \leq k_*$, the slope becomes $b = 0$, as found, for example, for MHD turbulence in refs. [38, 43, 44]. The peak wave number is chosen to be $k_* = 10$, followed by the slope in the UV range as $k^{-\frac{11}{3}}$, set by $c = \frac{11}{3}$. This corresponds to the spectrum obtained for Kolmogorov-like MHD turbulence [38]. Note, however, that this part of the spectrum corresponds to subhorizon scales, which are described accurately by the WKB approximation and, hence, the resulting spectral shape is not expected to be modified in this range. On the other hand, around the horizon or at larger scales, depending on the value of $\alpha_{\rm M}^{*}$, the resulting GW spectral shape might be modified by the inclusion of an additional IR branch $\xi^{\rm WKB}(k) \sim k^{-2}$ as predicted in section 3.3 by the WKB approximation. Finally, the resulting spectrum is expected to be enhanced at all wave numbers by a factor $e^{-2\mathcal{D}}(1 + \frac{1}{2}\alpha_{\rm T})$ owing to the presence of non-zero Horndeski parameters $\alpha_{\rm M}$ and $\alpha_{\rm T}$. Figure 2 shows the resulting GW spectrum estimated using the WKB approximation for different values of $\alpha_{\rm M}^{*}$. Note, however, that the assumptions made by the WKB approximation break down around the critical wave number at which we expect the relevant spectral modifications.

Table 1 summarizes the parameters of the runs for the numerical studies. The values of $\alpha_{\rm T,0}$ are chosen to be much larger than the current constraints in order to later show the relative insignificance of $\alpha_{\rm T,0}$ even with unrealistically large values. The choices of $\alpha_{\rm M,0}$ are made in line with the limits discussed in section 4.

For series T0 (T0A–T0D), we evolve the solution entirely with increasing time steps, such that $\eta_{\rm next} = \eta_{\rm current}(1 + \delta n_{\rm incr})$ with $\delta n_{\rm incr} = 0.01$, leading to equidistant points in logarithmic time spacing. For series M0 (M0A–M0F), M1 (M1A–M1D), M2 (M2A–M2D),

	run	$\alpha_{\mathrm{M},0}$	n	$\alpha_{\mathrm{T},0}$	$\mathcal{E}_{\mathrm{GW}}/\mathcal{E}^*_{\mathrm{GW}}$
Choice 0 (α_{T})	T0A	0	–	-0.5	7.50×10^{-1}
	T0B	0	–	-0.2	9.00×10^{-1}
	T0C	0	–	0.2	1.10×10^{0}
	T0D	0	–	0.5	1.25×10^{0}
Choice 0 (α_{M})	M0A	-0.5	–	0	3.44×10^{7}
	M0B	-0.3	–	0	3.32×10^{4}
	M0C	-0.1	–	0	3.21×10^{1}
	M0D	-0.01	–	0	1.41×10^{0}
	M0E	0.1	–	0	3.11×10^{-2}
	M0F	0.3	–	0	3.03×10^{-5}
Choice I (α_{M})	M1A	-0.5	2	0	1.28×10^{0}
	M1B	-0.3	2	0	1.16×10^{0}
	M1C	-0.1	2	0	1.05×10^{0}
	M1D	0.1	0.4	0	7.79×10^{-1}
	M1E	0.3	0.4	0	4.73×10^{-1}
Choice II (α_{M})	M2A	-0.5	–	0	1.32×10^{0}
	M2B	-0.3	–	0	1.18×10^{0}
	M2C	-0.1	–	0	1.06×10^{0}
	M2D	0.1	–	0	9.46×10^{-1}
	M2E	0.3	–	0	8.47×10^{-1}
Choice III (α_{M})	M3A	-0.5	–	0	3.57×10^{8}
	M3B	-0.3	–	0	1.35×10^{5}
	M3C	-0.1	–	0	5.12×10^{1}
	M3D	-0.01	–	0	1.48×10^{0}
	M3E	0.1	–	0	1.95×10^{-2}
	M3F	0.3	–	0	7.48×10^{-6}

Table 1: Parameters used for the numerical studies: for all runs, $k_1 = 10^{-3}$ is the smallest wave number and $N = 46\,000$ is the number of grid points in one dimension. $\mathcal{E}_{\mathrm{GW}}/\mathcal{E}^*_{\mathrm{GW}}$ indicates the present-day values of the energy density due to modified gravity with respect to the corresponding GR values. For each of the runs in series M0 and M3, we have performed an additional run with $k_1 = 10^{-7}$ to study the spectral modifications at even smaller k.

and M3 (M3A–M3F), we keep the nonuniform time scheme during RD and MD but switch to linear time steps during ΛD such that $\eta_{\mathrm{next}} = \eta_{\mathrm{current}} + \delta\eta$ with $\delta\eta\,\mathcal{H}_* = 5 \times 10^9$. We chose such time evolutions to improve the accuracy of late-time results for reduced Horndeski models, especially the modifications that they present in the IR limit (see last column in table 1). We show in appendix B that decreasing the time step below $\delta\eta\,\mathcal{H}_* = 5 \times 10^9$ does not affect the IR range of the spectra, which indicates that the observed modifications are not due to numerical inaccuracy. Since series T0 does not exhibit k-dependent modifications, it does not require the additional computational effort. The choice of time schemes and their numerical accuracy is further discussed in appendix B.

In the simulations, we consider the initial time to be the EWPT with a temperature scale $T_* \sim 100\,\mathrm{GeV}$ and the number of relativistic and adiabatic DOFs are $g_{\mathrm{S}} \approx g_* \sim 100$, which yields the values of a_* and $\mathcal{H}_*$ in equations (2.15) and (2.16). With these values, we can then solve equation (2.5) in units of the normalized time $\eta\mathcal{H}_*$, by mapping the parameterizations

in equation (4.1) $\alpha_{\rm M}(\eta) \to \alpha_{\rm M}(\eta/\eta_*)$ and using the results from Friedmann equations for $\mathcal{H}$ and a''/a (which are already normalized since a' is computed as the derivative with respect to $\eta\mathcal{H}_*$), given in equation (2.12). The effects on $S_{h'}(k,\eta)$ of the specific choice of the time at which the GWs are generated only appear via the relative magnitude of the terms a''/a and $\alpha'_{\rm M}$ that involve time derivatives (normalized by $\mathcal{H}_*$) compared to k. These terms have been parameterized in equations (3.11) and (4.3), respectively, and their magnitude has been discussed. We have shown that the term a''/a can only induce modifications to the solution at scales several orders of magnitude above the horizon scale, while $\alpha'_{\rm M}$ is only of the order of $\alpha_{\rm M}$ for choice III (see section 4) at very late times within the RD era. For other choices of $\alpha_{\rm M}(\eta)$, either $\alpha'_{\rm M} = 0$ (choice 0) or $\alpha_{\rm M}$ itself is orders of magnitude below its present-time value $\alpha_{\rm M,0}$ (choices I and II). We find that the WKB approximation is expected to be valid around $k \gg k_{\rm lim,\,\alpha_{\rm M}} \sim \sqrt{|\alpha^*_{\rm M}|/2}$ and, on the other hand, it predicts an enhancement k^{-2} in the IR regime $k \lesssim k_{\rm crit} \leq k_{\rm lim,\,\alpha_{\rm M}}$, which is not on the range of validity of the WKB estimate. Using the results of the numerical simulations, we find in section 5.3 an IR enhancement $\xi(k) \propto k^{-\beta_0}$ with $\beta_0 \sim 2$ and $\beta_0 \gtrsim 0$ for negative and positive values of $\alpha_{\rm M,0}$, respectively, that does not in general follow the spectral shape predicted by WKB and that can become shallower at smaller k. The position of this spectral change is a fixed fraction of the Hubble horizon at the time of generation, determined by the value of $\alpha^*_{\rm M}$, that does not depend on the specific value of η_*. Finally, the time of generation determines the range of frequencies where we observe the signal as well as its amplitude via equation (3.15).

The peak amplitude $S^*_{h'}$ can be chosen to represent a specific model. For example, a value of $S^*_{h'} = 3.5 \times 10^{-10}$ is used in our runs (see table 1) and it would produce a normalized initial total energy density[8] $\mathcal{E}^*_{\rm GW} \simeq 10^{-9}$, which corresponds to a vortically turbulent source energy density of roughly $q\mathcal{E}^*_{\rm turb} \simeq 1.74 \times 10^{-4}$. This is related via

$$\mathcal{E}^*_{\rm GW} = (q\mathcal{E}^*_{\rm turb}/k_{\rm s})^2, \tag{5.3}$$

where q is an empirically determined coefficient for a specific type of turbulence source $\mathcal{E}^*_{\rm turb}$, and is found to be of the order of unity or larger (up to ~ 5), depending on the production mechanism of the source [38, 40, 41], and $k_{\rm s}$ is the characteristic scale of the turbulence sourcing, which is related to k_* in equation (5.1) as $k_* \simeq 1.143 \cdot 1.6\, k_{\rm s} \simeq 1.83\, k_{\rm s}$, where the factor 1.143 relates the position of the maximum of $\Omega_{\rm GW}(k) \propto k S_{h'}(k)$ and k_*, and 1.6 the relation between $k_{\rm s}$ and the maximum [43].

5.2 Time evolution

For constant $\alpha_{\rm T} \neq 0$ and $\alpha_{\rm M} = 0$, the GW energy density stays constant in time and its magnitude is modified by the specific value of $\alpha_{\rm T}$, as it can be predicted from the analytical solution to equation (2.5) in the absence of sources during RD, given in equations (3.9) and (3.20) under the WKB approximation. We find excellent agreement between the WKB estimate and the numerical solution of the GW energy density. Note that this corresponds to a boost of energy for $\alpha_{\rm T} > 0$ and a depletion for $\alpha_{\rm T} < 0$, given by $1 + \alpha_{\rm T}/2$. Hence, the relative changes upon the GR solutions are of order $\alpha_{\rm T} \sim \mathcal{O}(10^{-1})$ (see table 1), which would

[8] The turbulent and GW energy densities are normalized to the radiation energy density, such that $\mathcal{E}_{\rm GW}$ during RD can be computed as

$$\mathcal{E}_{\rm GW}(\eta) = \frac{1}{6}\int_0^\infty S_{h'}(k,\eta)\,{\rm d}k. \tag{5.2}$$

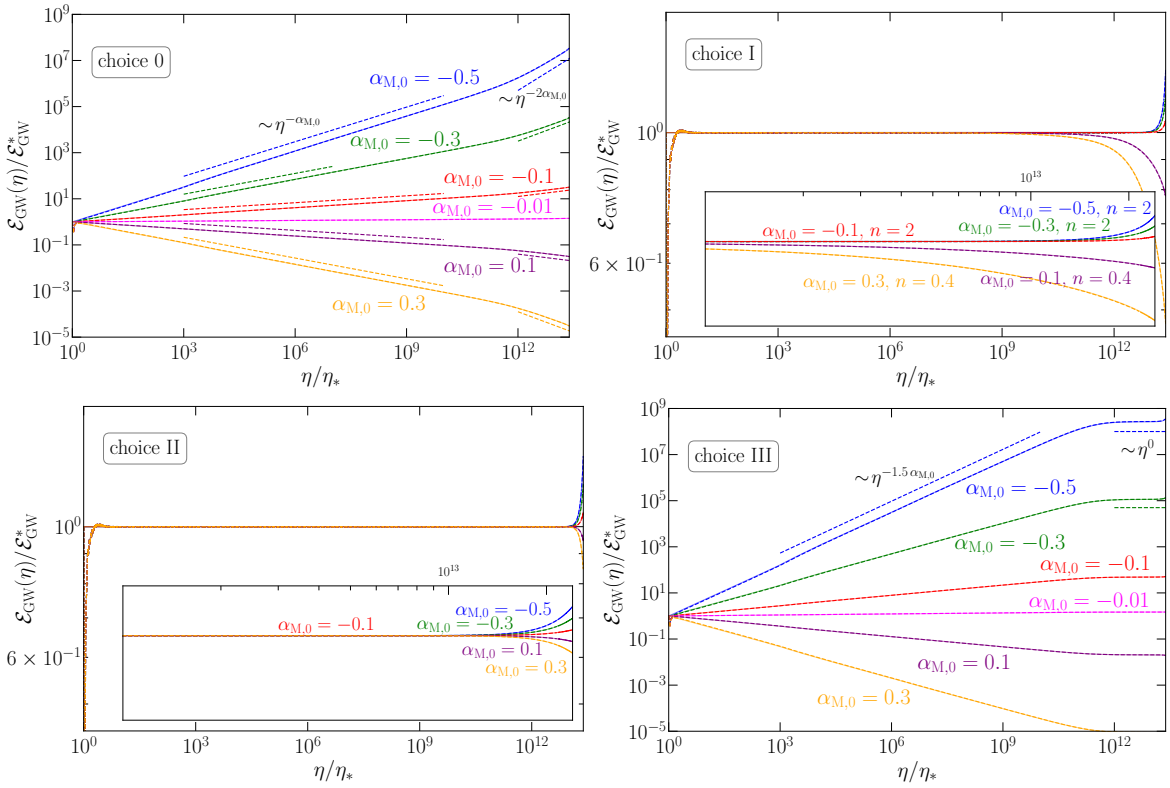

Figure 3: Time evolution of the normalized total energy density $\mathcal{E}_{\rm GW}/\mathcal{E}^*_{\rm GW}$ for choices 0 to III and $\alpha_{\rm M,0} \in \{-0.5, -0.3, -0.1, -0.01, 0.1, 0.3\}$. In all panels, the WKB estimates are shown as solid lines and numerical solutions as dashed lines, being almost indistinguishable. For choices I and II, the inset corresponds to the ΛD era, when there are relevant modifications to the GR solution $\mathcal{E}^*_{\rm GW}$. All runs are initialized at the EWPT such that the present time is $\eta_0/\eta_* \simeq 2.4 \times 10^{13}$.

become much smaller if we restrict $\alpha_{\rm T}$ to the present-time constraint at the LIGO-Virgo frequency band $\alpha_{\rm T,0} \lesssim \mathcal{O}(10^{-15})$.

Figure 3 presents the time evolution of the total GW energy density $\mathcal{E}_{\rm GW}(\eta)$ of the runs in series M0 (upper left), M1 (upper right), M2 (lower left), and M3 (lower right). In these runs, $\alpha_{\rm M}$ follows each of the parameterizations given in equation (4.1) and $\alpha_{\rm T} = 0$. The numerical solutions and the WKB approximations agree on the total GW energy density time dependence, enhanced or depleted by a factor $e^{-2\mathcal{D}}$. Regardless of the specific parameterization, we find an enhancement or a suppression of $\mathcal{E}_{\rm GW}$ over time for negative or positive values of $\alpha_{\rm M,0}$, respectively.

Choices 0 and III yield similar results, with a time evolution $\mathcal{E}_{\rm GW}(\eta) \sim \eta^{-\alpha_{\rm M,0}}$ and $\mathcal{E}_{\rm GW}(\eta) \sim \eta^{-1.5\,\alpha_{\rm M,0}}$ during RD era, and $\mathcal{E}_{\rm GW} \sim \eta^{-2\alpha_{\rm M,0}}$ and $\mathcal{E}_{\rm GW}(\eta) \sim \eta^0$ during MD, respectively. This agrees with the expectation since choice III mostly differs from choice 0 during MD. During RD, both parameterizations are almost the same and just differ by a factor $1/(1-\Omega_{\rm mat,0}) \simeq 1.46$, leading to the different scalings. In other words, the evolution of $\mathcal{E}_{\rm GW}$, proportional to $a^{-\alpha_{\rm M}}$ when $\alpha_{\rm M}$ is constant (e.g., for choice 0, and for choice III during RD era), is determined by the cosmic expansion itself. Note that choices 0 and III induce an enhancement or suppression in the total energy density that heavily depends on

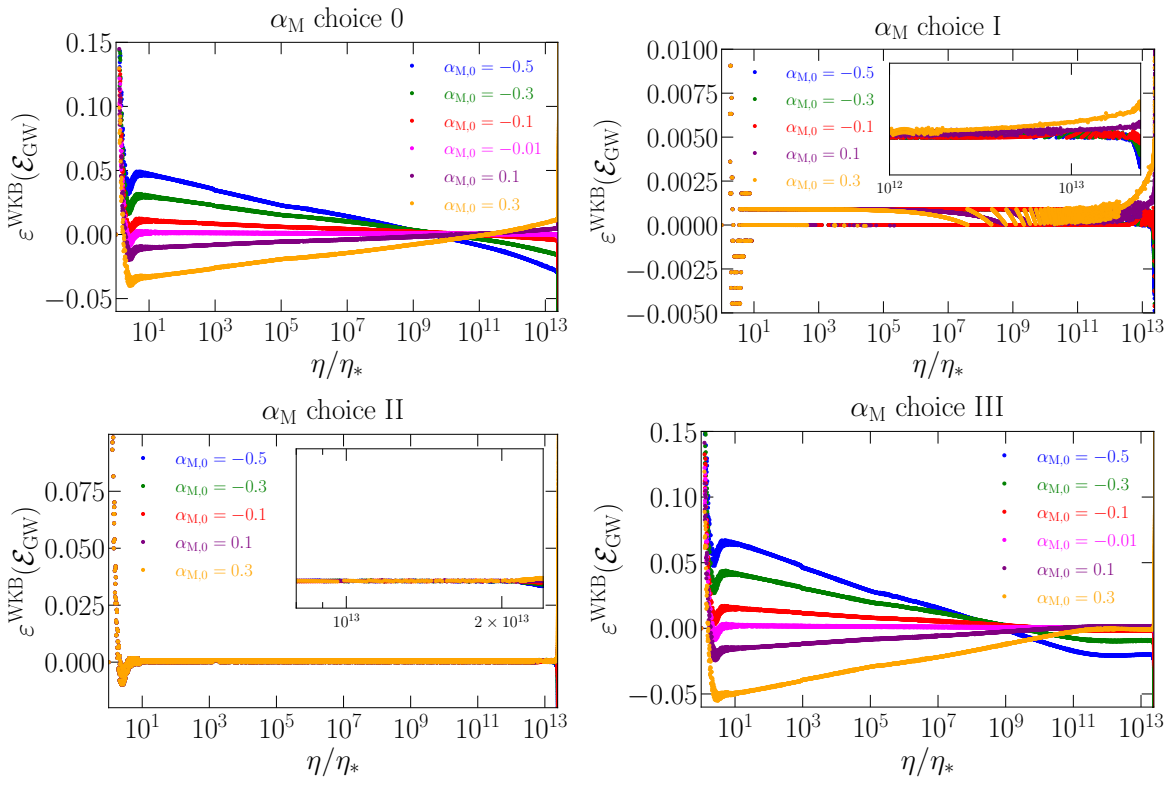

Figure 4: Relative error on the time series in figure 3 of the WKB approximation compared to the numerical simulations, $\varepsilon^{\rm WKB}(\mathcal{E}_{\rm GW})$.

the values of $\alpha_{\rm M,0}$, i.e., $\mathcal{E}_{\rm GW}/\mathcal{E}^*_{\rm GW}$ can range from $\mathcal{O}(10^{-5})$ (choice 0) and $\mathcal{O}(10^{-6})$ (choice III) for $\alpha_{\rm M,0} = 0.3$ to $\mathcal{O}(10^{7})$ (choice 0) and $\mathcal{O}(10^{8})$ (choice III) for $\alpha_{\rm M,0} = -0.5$. In general, choice III leads to a larger modification due to larger values of $\alpha_{\rm M}$ during RD than choice 0. The potential implications of such a large GW energy density enhancement are discussed in section 6.

For both choices I and II (see the upper right and lower left panels of figure 3), the modified GW solutions remain close to their GR counterparts for most of the time, and rapidly depart from GR as η enters ΛD and approaches the present day. This is expected since $\alpha_{\rm M}$ is proportional to the scale factor and the dark energy density for choices I and II, respectively, and hence, the values of $\alpha_{\rm M}$ are negligibly small for most of the cosmic history until ΛD era. For this reason, for the same values of $\alpha_{\rm M,0}$, the final values of $\mathcal{E}_{\rm GW}$ in both of these cases are significantly lower than those in choices 0 and III, where the modifications are accumulated from RD onward.

In figure 3, the differences between the WKB and the numerical solutions are indistinguishable. We quantify in figure 4 the relative error between the two, defined to be $\varepsilon^{\rm WKB}(\mathcal{E}_{\rm GW}) \equiv [\mathcal{E}^{\rm WKB}_{\rm GW}(\eta) - \mathcal{E}_{\rm GW}(\eta)]/\mathcal{E}_{\rm GW}(\eta)$. In all panels, there exists a brief but relative large error region, amounting to $\lesssim 15\%$, around the initial time η_*. This is due to the sinusoidal oscillations of each k mode that are present in GR and modified gravity alike [see equations (3.7) and (3.8)]. It is a consequence of setting an already saturated spectra $S_{h'}(k)$ as the initial condition at time η_* and hence, it is not due to the WKB estimate. After the initial oscillations settle down, $\varepsilon^{\rm WKB}(\mathcal{E}_{\rm GW})$ for choices 0 and III decrease over the majority

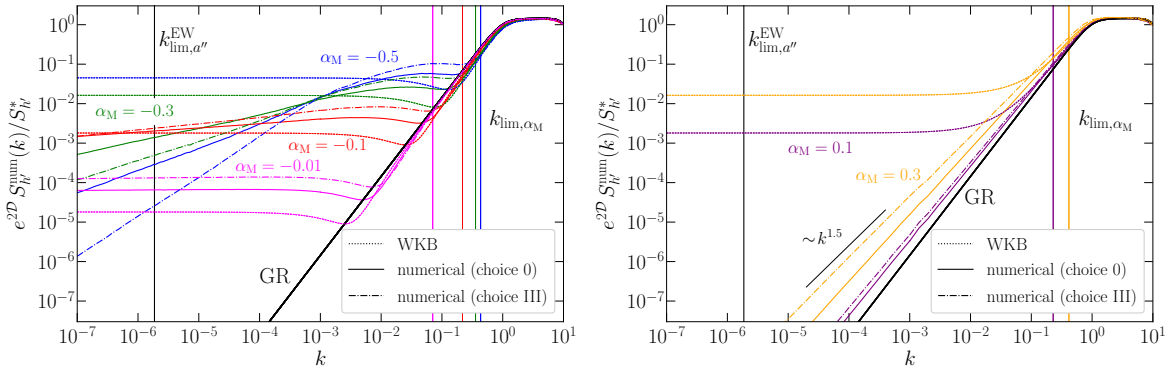

Figure 5: Saturated final energy spectra compensated by the change on the total GW energy density $e^{2\mathcal{D}} S^{\rm num}_{h'}(k)/S^*_{h'}$ for the numerical runs with the choices 0 and III of $\alpha_{\rm M}$ parameterization. Left and right panels represent negative and positive values of $\alpha_{{\rm M},0}$, respectively. The GR solution and WKB approximation are shown in black solid and color dashed lines. Numerical solutions are shown in solid (choice 0) and dash-dotted (choice III) lines. Thin vertical lines indicate the corresponding limits to the WKB approximation $k^{\rm EW}_{{\rm lim},\,a''}$ and $k_{{\rm lim},\,\alpha_{\rm M}}$.

of time in RD era. Although they both increase somewhat later on, the maximum error at the final time is only $\varepsilon^{\rm WKB}(\mathcal{E}_{\rm GW}) \sim 3\%$. For choices I and II, due to the negligible impact of $\alpha_{\rm M}$ during RD, the GW solutions settle down to the same magnitude after the initial oscillations. Therefore, the relative errors during RD remain close to zero. During ΛD, the errors grow as the effects of $\alpha_{\rm M}$ become more significant. But this is also limited, since at most $\varepsilon^{\rm WKB}(\mathcal{E}_{\rm GW}) \sim 1\%$ is found at the present day, lower than in choices 0 and III.

5.3 Energy spectrum

In figure 5, we show the final energy spectrum averaged over oscillations and compensated by the factor $e^{-2\mathcal{D}}$ to study the changes on the spectral shape. The saturated spectra are shown for the choices 0 and III of $\alpha_{\rm M}$ parameterization, since the rest of runs ($\alpha_{\rm T}$ choice 0, $\alpha_{\rm M}$ choices I and II) exhibit the same spectral shape as in GR. To study the spectral changes, we again define $\xi(k) = e^{2\mathcal{D}} S_{h'}(k)/S^{\rm GR}_{h'}(k)$, in analogy to equation (3.18). As a reminder of the potential limitations of the WKB approximation, we mark with thin vertical lines the values of $k^{\rm EW}_{{\rm lim},\,a''}$ and $k_{{\rm lim},\,\alpha_{\rm M}}$, and note that the latter occurs at wave numbers larger than the IR regime characterized by $k_{\rm crit} = \frac{1}{2}|\alpha^*_{\rm M}|$.

Comparing the numerical results to the expected spectra obtained using the WKB approximation (see figure 2), we note two main differences. In the first place, the IR enhancement $\xi(k) \sim k^{-\beta_0}$ with $\beta_0 \in (1, 2)$ found under the WKB approximation (where $\beta_0 = 2$ is found) only appears for negative values of $\alpha_{{\rm M},0}$ whereas for positive values there are more moderate modifications with β_0 up to 0.5, to the spectral shape. Moreover, even for negative $\alpha_{{\rm M},0}$, the modifications to the spectral shape are different than those predicted by the WKB estimate. These modifications can be seen more clearly in figure 6, where the left panel shows the numerically obtained $\xi(k)$ and the right panel directly presents the spectral slopes of the compensated spectra $\beta \equiv -\partial \log \xi(k)/\partial \log k$, measured at each wave number.

The slope β of the WKB estimate can be computed as

$$\beta = \frac{2\alpha^*_{\rm M}\left(\alpha^*_{\rm M} + 2k\right)}{8k^2 + \alpha^{*2}_{\rm M} + 4k\alpha^*_{\rm M}}, \tag{5.4}$$

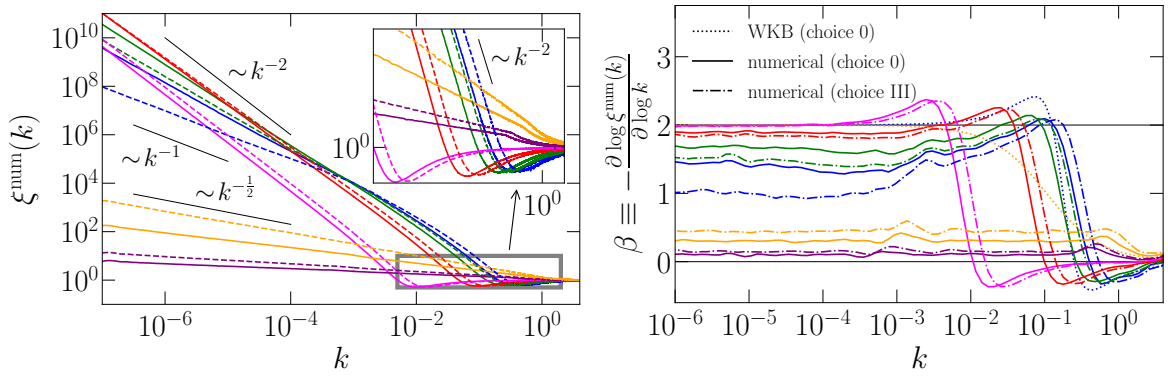

Figure 6: Left and right panels respectively show $\xi^{\rm num}(k)$, the saturated spectra normalized with the GR solution, and β, its spectral slope as a function of wave number. We show, for comparison, the slopes β predicted by the WKB estimate for $\alpha_{\rm M,0} = -0.5$ and 0.3. The horizontal thin black lines in the right panel indicate the slopes 0 and 2 for reference. Different values of $\alpha_{\rm M,0}$ and line colors are consistent with the ones used in figures 3–5.

which has an initial departure $\beta < 0$ for $\alpha_{\rm M}^* < 0$ as k decreases until it reaches a peak $\beta_{\rm min} = 1 - \sqrt{2} \simeq -0.41$ at $k_{\beta_{\rm min}} = \frac{1}{4}\alpha_{\rm M}^*\sqrt{2}/(1-\sqrt{2}) \simeq 0.85\,|\alpha_{\rm M}^*|$. It then grows again to zero at $k_{\rm crit}$ and continues to increase up to $\beta_{\rm max} = 1 + \sqrt{2} \simeq 2.41$ at $k_{\beta_{\rm max}} = -\frac{1}{4}\alpha_{\rm M}^*\sqrt{2}/(1+\sqrt{2}) \simeq 0.15\,|\alpha_{\rm M}^*|$, crossing the aforementioned IR enhanced slope of -2 at the wave number $k_{\beta=2} = \frac{1}{4}|\alpha_{\rm M}^*|$. Finally, the slope becomes slightly shallower and asymptotically tends to -2 as $k \to 0$, as can be seen by taking the limit in equation (5.4). For positive values of $\alpha_{\rm M}^*$, the slope β monotonically increases from 0 to 2 with decreasing k so it does not present any local minima or maxima. The slope β for $\alpha_{\rm M}^* = -0.5$ and 0.3 under the WKB estimate is shown in the right panel of figure 6 for comparison with the numerical results.

At wave numbers close to where the IR regime starts, $k \lesssim k_{\rm crit}$, the k^{-2} enhancement is reproduced by the numerical results for negative $\alpha_{\rm M,0}$, flattening that part of the original GR spectrum to k^0 (see figure 5). But as k decreases, the numerical spectra exhibit slopes steeper than k^0, closer to the original GR k^2 spectrum, that are not predicted by the WKB approximation, which maintains the k^0 slope throughout all scales $k \lesssim k_{\rm crit}$. The departure in the IR regime occurs at different scales depending on the values of $\alpha_{\rm M,0}$. For $\alpha_{\rm M,0} = -0.01$, this is the least obvious, where the enhanced spectrum still keeps a roughly k^0 shape even at $k \ll k_{\rm crit}$. For $\alpha_{\rm M,0} = -0.5$, however, the difference becomes visible when k is still relatively close to the start of the IR regime at $k \sim k_{\rm crit}$. We characterize the differences of the numerical results with those from the WKB estimate in table 2 by computing the critical k at which $\beta = 2$, $k_{\beta=2}^{\rm crit}$. Under WKB this only occurs at $\frac{1}{4}|\alpha_{\rm M}^*|$ and in the limit $k \to 0$ while in the simulations it occurs at a similar k and then again at a larger but finite scale $k_{\beta=2}^{\rm crit,2}$, when the spectra becomes steeper (with respect to the flat spectrum induced by $\xi(k) \sim k^{-2}$). We also give the final slope β_0, such that $\xi(k) \sim k^{-\beta_0}$ as $k \to 0$.

On the other hand, for positive $\alpha_{\rm M,0}$, the behavior predicted by the WKB estimate is not observed in the numerical results. In this case, the modified spectra present small increases around $k \gtrsim 1$ and slightly shallower slopes than their GR counterparts at all superhorizon scales, characterized by $\beta_0 \gtrsim 0$.

Finally, to quantify the departures of the WKB approximation from the numerical solutions, especially at $k \leq k_{{\rm lim},\alpha_{\rm M}}$, we show the relative errors in the saturated spectra as

	$\alpha_{\rm M,0}$	WKB	Choice 0 ($\alpha_{\rm M}$)	Choice III ($\alpha_{\rm M}$)
$k^{\rm crit}_{\beta=2}$	-0.5	1.25×10^{-1}	1.32×10^{-1}	1.79×10^{-1}
	-0.3	7.5×10^{-2}	9.04×10^{-2}	1.20×10^{-1}
	-0.1	2.5×10^{-2}	3.83×10^{-2}	5.16×10^{-2}
	-0.01	2.5×10^{-3}	4.58×10^{-3}	6.63×10^{-3}
$k^{\rm crit,2}_{\beta=2}$	-0.5	0	6.73×10^{-2}	9.93×10^{-2}
	-0.3	0	3.09×10^{-2}	5.54×10^{-2}
	-0.1	0	4.42×10^{-3}	9.62×10^{-3}
	-0.01	0	5.04×10^{-5}	7.44×10^{-5}
β_0	-0.5	2	1.38	0.95
	-0.3	2	1.66	1.47
	-0.1	2	1.89	1.84
	-0.01	2	2.00	1.99
	0.1	2	0.10	0.15
	0.3	2	0.30	0.44

Table 2: Spectral features in the IR regime for the values of $\alpha_{\rm M,0}$ used in the numerical runs of table 1 and for choices 0 and III. $k^{\rm crit}_{\beta=2}$ and $k^{\rm crit,2}_{\beta=2}$ indicate the wave numbers at which the spectral slope becomes -2, which occurs at $k_{\beta=2}=\{0,\frac{1}{4}|\alpha^*_{\rm M}|\}$ for the WKB estimate. β_0 is the asymptotic slope in the numerical runs, such that $\xi(k)\sim k^{-\beta_0}$ at large scales, which corresponds to $\beta_0=2$ for the WKB estimate.

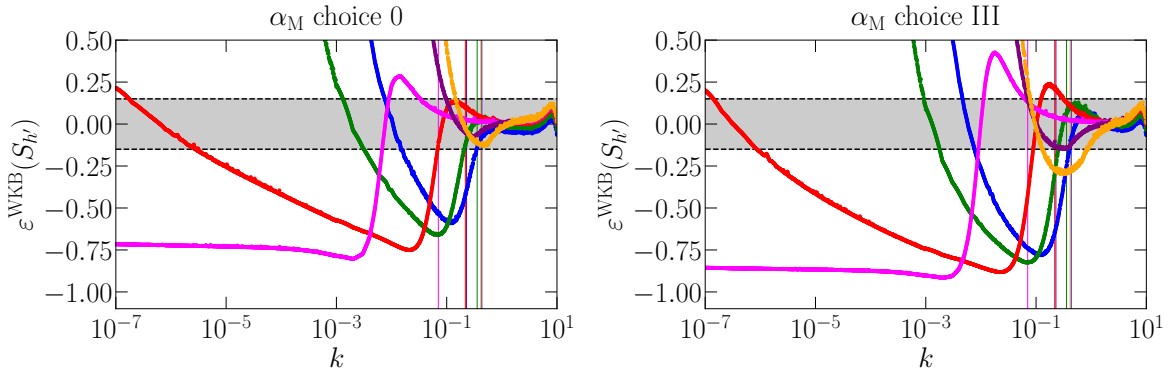

Figure 7: Relative error $\varepsilon^{\rm WKB}(S_{h'})$ in the saturated spectra at late times of the WKB approximation compared to the numerical simulations. The vertical lines correspond to the wave number $k_{\rm lim,\,\alpha_M}$, below which the WKB estimate is expected to break down. The gray shaded regions in both panels represent relative errors of $\leq 15\%$. Different values of $\alpha_{\rm M,0}$ and line colors are consistent with the ones used in figures 3–5.

$\varepsilon^{\rm WKB}(S_{h'})\equiv[S_{h'}(k)^{\rm WKB}-S_{h'}(k)]/S_{h'}(k)$ in figure 7. We observe that for positive values of $\alpha_{\rm M,0}$, the errors grow monotonically as k becomes smaller. In fact, $\varepsilon^{\rm WKB}(S_{h'})\sim k^{-2}$ is found due to a consistent disagreement between the flat spectra predicted by the WKB formalism and $k^{2-\beta_0}$ with $\beta_0\gtrsim 0$ obtained numerically (see table 2). On the other hand, for negative values of $\alpha_{\rm M,0}$, $\varepsilon^{\rm WKB}(S_{h'})$ also increase as k becomes smaller. But since $\alpha_{\rm M,0}<0$ still produces a similar IR enhancement than that predicted by the WKB, the slope in the error spectrum does not become as steep as k^{-2} and depends on the corresponding values of

β_0 in table 2. In all of the runs, the errors are bounded by $\lesssim 15\%$ at $k \gtrsim k_{\mathrm{lim},\,\alpha_{\mathrm{M}}}$, where the WKB estimate is expected to be valid.

6 Observational implications

To infer the observational prospects of detecting a modified GW background, we convert the linear energy spectrum $S_{h'}(k)$ directly obtained from the code to the commonly used logarithmic energy spectrum $\Omega_{\mathrm{GW}}(f)$ via equation (3.15). As a result, the GR solution in the form of the double broken power law used in the numerical simulations, i.e., $S_{h'}(k) \propto k^2$, k^0, and $k^{-\frac{11}{3}}$ in the low, intermediate, and high wave number regimes, given by the smoothed double broken power law in equation (5.1), becomes $\Omega_{\mathrm{GW}}(f) \propto f^3$, f, and $f^{-\frac{8}{3}}$, respectively. The normalized wave numbers used in the code are converted to the present-day physical frequencies via

$$f = \frac{k\mathcal{H}_*}{2\pi}\,\frac{a_*}{a_0}, \tag{6.1}$$

where $\mathcal{H}_*$ and a_*/a_0 are given in equations (2.15) and (2.16) and depend on the time at which the GWs are generated.

Assuming that the origin of the GWs is the EWPT and that the characteristic scale of the source is $\mathcal{H}_*\lambda_{\mathrm{s}} = 10^{-2}$ (given, for example, by the mean separation of the broken-phase bubbles in a first-order EWPT [61]), then $\Omega_{\mathrm{GW}}(f)$ today peaks around the mHz band, which corresponds to the peak sensitivity of the Laser Interferometer Space Antenna (LISA). On the other hand, if the GW signal is produced at the QCDPT with a characteristic length scale of the order of the Hubble scale $\mathcal{H}_*\lambda_{\mathrm{s}} \approx 1$, then it would be compatible [43] with the recent observations by the different pulsar timing array (PTA) collaborations [62–65] in the nHz band of frequencies, which are, however, not yet confirmed to correspond to a GW background. In particular, for a signal produced from MHD turbulence, the peak is estimated to occur at $k_{\mathrm{GW}} \simeq 1.6 \times 2\pi/(\mathcal{H}_*\lambda_{\mathrm{s}})$ [43], which is obtained by taking $k_* \simeq 0.875\, k_{\mathrm{GW}}$ in equation (5.1).

Choosing the cases with the most pronounced modifications, we show in figure 8 the resulting $\Omega_{\mathrm{GW}}(f)$ of the runs using the choice III of α_{M} parameterizations, i.e., the runs of series M3; see table 1, for the cases in which the GW signal is produced at the EWPT and at the QCDPT. For observational comparisons, we show the power law integrated sensitivity (PLIS) curves [66] of proposed future detectors such as Square Kilometer Array (SKA) [67], DECi-hertz Interferometer Gravitational wave Observatory (DECIGO) [68], Big Bang Observer [69], LISA [34], and Einstein Telescope (ET) [70].

Due to the factor $e^{-2\mathcal{D}}$, negative values of $\alpha_{\mathrm{M},0}$ boost the GW spectral amplitude, which increases the chance of GW detection. Hence, the (non-)observation of a GW signal could serve as a constraint on the value of $\alpha_{\mathrm{M},0}$. However, the present-day amplitude of the GW spectrum is degenerate with respect to the value of $e^{-2\mathcal{D}}$ at present time (shown in figure 9, it depends on $\alpha_{\mathrm{M},0}$, the time-dependent parameterization of α_{M}, and the time of generation of the GWs) as well as the GW energy density produced at the time of generation $\mathcal{E}^*_{\mathrm{GW}}$. We show in figure 8 for different values of $\alpha_{\mathrm{M},0}$ the expected spectra at present time obtained for fixed values $e^{-2\mathcal{D}}(\eta_0)\,\mathcal{E}^*_{\mathrm{GW}} \simeq 2.5 \times 10^{-7}$ and 4.44×10^{-1} at the EWPT with $k_{\mathrm{s}} \simeq 600$, which correspond to the spectral peaks at present time $h^2\,\Omega_{\mathrm{GW}} \simeq 2.34 \times 10^{-12}$ and 4.15×10^{-6} at 2.5 mHz. Note that the former amplitude would correspond to $q\mathcal{E}^*_{\mathrm{turb}} \simeq 0.3$ in GR while the latter would be $q\mathcal{E}^*_{\mathrm{turb}} \simeq 400$, which is completely unrealistic, but in modified GR, this would be compatible with $q\mathcal{E}^*_{\mathrm{turb}} \simeq 0.3$ again if $e^{-2\mathcal{D}}(\eta_0) \simeq 2 \times 10^6$ that can be obtained if $\alpha_{\mathrm{M},0} \approx -0.3$ (see figure 9). In this case, the GW signal could be amplified by

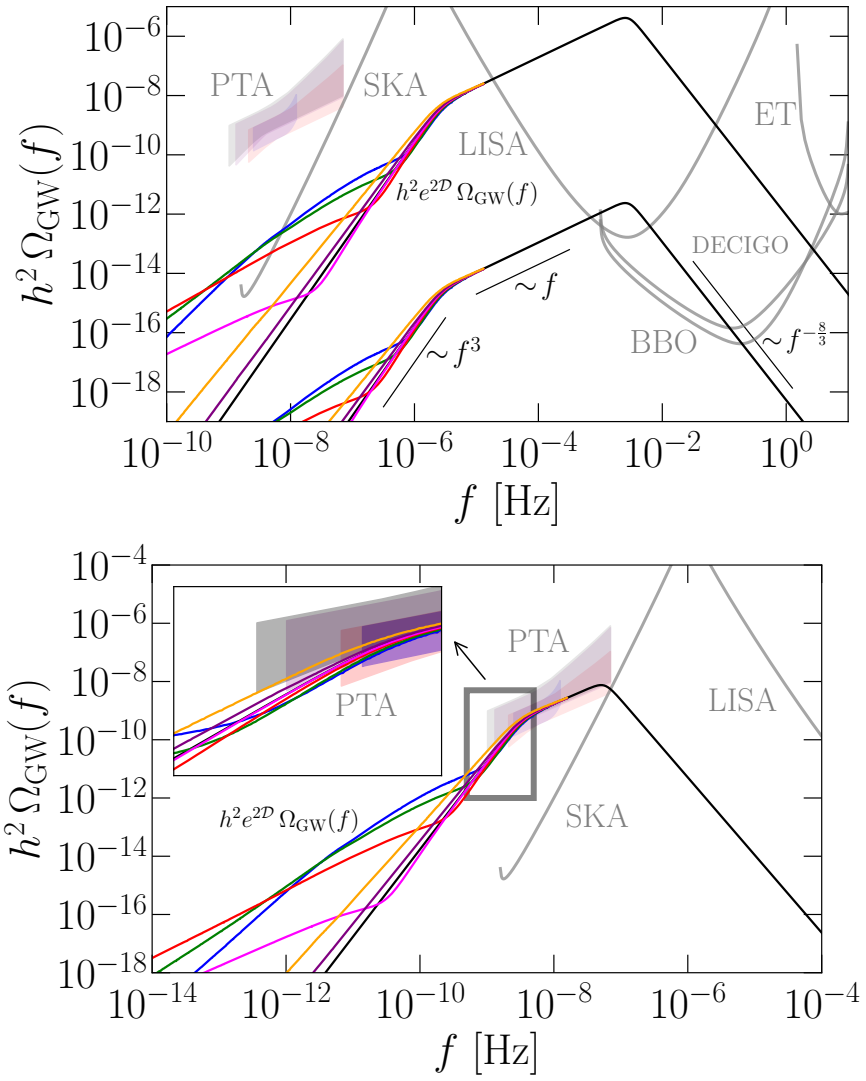

Figure 8: Present-day modified GW energy spectrum for the numerical runs of series M3 (see table 1) for GW signals produced at the EWPT (upper panel) and at the QCDPT (lower panel). GR solution is shown in black. Different values of $\alpha_{\rm M,0}$ and line colors are consistent with the ones used in figures 3–5. Several detectors' PLIS curves for a signal-to-noise ratio of 10 are shown in gray for comparison. The recent PTA reported observations are shown as shaded regions in blue (NANOGrav), red (PPTA), purple (EPTA), and black (IPTA) for their 2σ confidence amplitudes in the range of slopes $\gamma \geq 0$ for $\Omega(f) \sim f^{\gamma}$.

modifications of gravity such that the low-frequency tail could become detectable by SKA and the different PTA collaborations in the future, in a way that would break the degeneracy by a potential observation over different frequency bands. At the nHz frequencies, the f^3 branch is modified to a different slope that depends on the value of $\alpha_{\rm M}^*$ at the time of generation, yielding a potential indirect observation of the Horndeski parameter during RD era. The non-observation of such a signal at nHz frequencies would similarly constrain the value of $\alpha_{\rm M}^*$ if a compatible signal is observed by LISA. Otherwise, only the product $e^{-2\mathcal{D}}(\eta_0)\,\mathcal{E}_{\rm GW}^*$ could be constrained by not detecting such a signal in the LISA band. Similarly, an even

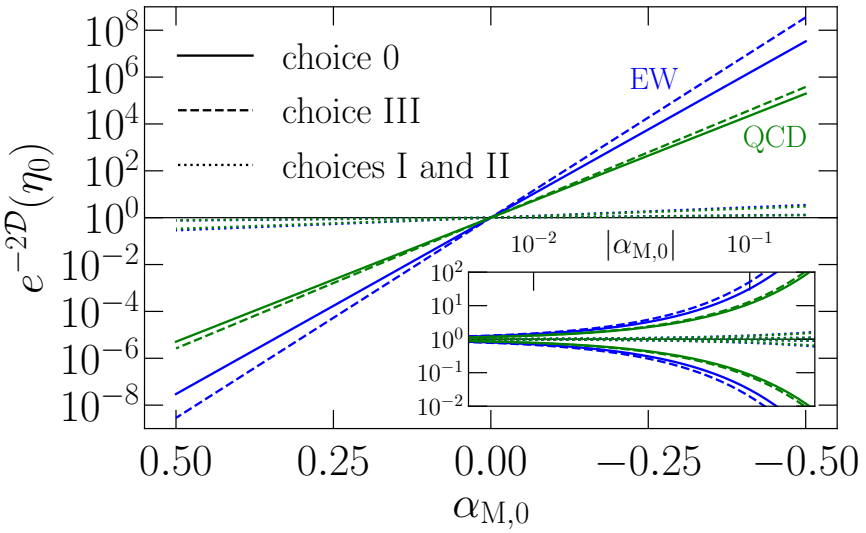

Figure 9: Total amplification or depletion factor as a function of $\alpha_{\rm M,0}$ for a GW signal produced at the EWPT (blue) and at the QCDPT (green) for the different choices of $\alpha_{\rm M}$ parameterization in equation (4.1).

larger amplification $e^{-2\mathcal{D}}(\eta_0)\,\mathcal{E}^*_{\rm GW} \simeq 50$ could in principle allow the large frequency branch $f^{-8/3}$ to fall into ET sensitivity. Hence, ET could also be used to put upper bounds on the amplifications, although less stringent than the other ones.

For the QCDPT, we take the fixed value $e^{-2\mathcal{D}}(\eta_0)\,\mathcal{E}^*_{\rm GW} \simeq 5\times10^{-4}$ with $k_{\rm s} \simeq 10$, which corresponds to a spectral peak $h^2\,\Omega_{\rm GW} \simeq 7.4\times10^{-9}$ at 50.6 nHz. In GR, this corresponds to $q\mathcal{E}^*_{\rm turb} \simeq 0.22$ so it is compatible with, for example, the primordial magnetic fields proposed in refs. [42, 43, 71] in connection to the reported PTA observations. In this case, the horizon at the QCDPT scale is within the range of frequencies where PTAs are sensitive and hence, the amplitude can be slightly modified by the value of $\alpha^*_{\rm M}$ at the time of generation. Such modifications are small and at the moment, the data is not accurate enough for such a precision measurement. However, this is an interesting feature that occurs around the horizon and the potential observation of a deviation with respect to the GR spectrum around the horizon scale could be an indication of non-zero $\alpha^*_{\rm M}$ around the QCD scale. On the other hand, the current PTA observations allow us to constrain the product $e^{-2\mathcal{D}}\mathcal{E}^*_{\rm GW}$ for different values of $k_{\rm s}$ since we can find their values at which the GW signal would be larger than the reported PTA common-noise observations: $e^{-2\mathcal{D}}\mathcal{E}^*_{\rm GW} \leq 2.5\times10^{-3}$ for $k_{\rm s}\approx 10$, $\leq 2.5\times10^{-2}$ for $k_{\rm s}\approx 60$, $\leq 4\times10^{-2}$ for $k_{\rm s}\approx 100$, $\leq 2.5\times10^{-1}$ for $k_{\rm s}\approx 600$.

In addition, the expected value of $\mathcal{E}^*_{\rm GW}$ depends on the mechanisms leading to GW production, in particular, their efficiency q, which presents a fair amount of uncertainty. Recall equation (5.3), which states that the initial GW energy is determined by the initial turbulent source energy $\mathcal{E}^*_{\rm turb}$, the production efficiency q, and the characteristic size of turbulent eddies $k_{\rm s}$. Therefore, in practice, constraining $\alpha_{\rm M,0}$ via its amplification effects can be rather challenging.

Finally, we note that large amplifications due to modified gravity could potentially lead to GW signals produced at the EWPT that would dominate the sensitivity budget of various detectors, mostly LISA, but also DECIGO and BBO, for example if the product $e^{-2\mathcal{D}}(\eta_0)\,\mathcal{E}^*_{\rm GW} \sim 10^{-1}$ (see figure 8). Hence, at the moment that GW signals of astrophysical

origin that propagate over a shorter period of cosmic history are detected by LISA, DECIGO and/or BBO, then one can put upper bounds to $e^{-2\mathcal{D}}(\eta_0)\,\mathcal{E}^*_{\rm GW}$.

7 Conclusions

GWs in modified gravity exhibit features in their energy spectra different from what can be expected from GR. We have explored the significance of such features in terms of the spectral slopes and amplitudes in different frequency ranges, under different time-dependent functional forms and values of two modification parameters—the running of effective Planck mass $\alpha_{\rm M}$ and the tensor speed excess $\alpha_{\rm T}$.

We have computed the expected GW energy density spectra using the WKB approximation, and have found that the GW energy density depends on the time evolution of $\alpha_{\rm T}$ and $\alpha_{\rm M}$, while its spectral shape only depends on $\alpha^*_{\rm M}$ at the time of GW generation. However, a number of limiting scales below which the WKB approximation might not hold have been identified in equations (3.12)–(3.14), motivating numerical studies to go beyond the WKB estimate, especially at superhorizon scales. For this purpose, we have performed numerical simulations using the Pencil Code to study the propagation of GWs along the history of the universe from their time of generation, assumed to be during the RD era, e.g., at the EWPT or at the QCDPT, until the present time.

The current-day value of the tensor speed excess is already tightly constrained by the precise measurement of the speed of GWs to $\alpha_{\rm T,0} \lesssim \mathcal{O}(10^{-15})$. In this paper, we have found that the modifications on the GW energy density spectra introduced by $\alpha_{\rm T}$ are negligible, even when $\alpha_{\rm T}$ takes larger values (as it might be allowed where it is not constrained, e.g., in the past or at frequencies out of the LIGO-Virgo band) and stays constant in frequency and time. On the other hand, $\alpha_{\rm M}$ effectively acts as an (anti-)damping term in the GW equation and can impart changes to the energy spectrum of GWs with potential implications to future observations. Considering sources of GWs at the EWPT and QCDPT, the present-day GW spectrum is expected to peak in the mHz and nHz frequency bands, respectively.

Compared to the standard GW spectra obtained in GR, the changes due to $\alpha_{\rm M}$ are characterized by an overall boost or depletion factor $e^{-2\mathcal{D}}$, where $\mathcal{D}$ is given in equation (3.4). However, the GW energy density at present time due to modified gravity is degenerate with the produced density at the time of generation $\mathcal{E}^*_{\rm GW}$. Therefore, potential observations or non-observations of the GW spectra by PTA, SKA, LISA, BBO, DECIGO, ET, or others, could only place bounds on the quantity $e^{-2\mathcal{D}}(\eta_0)\,\mathcal{E}^*_{\rm GW}$ and not on $\alpha^*_{\rm M}$ or $\mathcal{E}^*_{\rm GW}$ separately. For example, we have provided some upper bounds on $e^{-2\mathcal{D}}(\eta_0)\,\mathcal{E}^*_{\rm GW}$ using the reported observations of a common-process spectrum over several pulsars by the different PTA collaborations; see section 6.

In addition, the GW spectrum also presents spectral modifications $\xi(k)$ around the horizon and at superhorizon scales. If $\alpha_{\rm M} < 0$, then $\mathcal{D} < 0$ leads to an enhancement of the GW spectrum $\xi(k) \sim k^{-\beta}$ with $\beta \in (0, 2)$, which flattens the low- frequency part of the spectrum; see table 2. The enhancement found from the numerical simulations is different than the one predicted by the WKB estimate ($\beta = 2$) but it still increases the detection prospects of the low-frequency tail of the GW spectra.

The degeneracy between $\alpha_{\rm M}$ and $\mathcal{E}^*_{\rm GW}$ can be reduced by observing the signal at multiple frequency bands, as the former leads to a low-frequency spectral enhancement, while under GR such enhancement does not appear. This implies that, for example, a GW spectrum peaking in the mHz band can potentially have its tail in the nHz band, above PTA or SKA

sensitivities. The observation of such a low-frequency tail would then be a direct indication of a non-zero $\alpha_{\rm M}$ at the time at which the GW signal has been produced since the slope and amplitude would only depend on $\alpha_{\rm M}^*$.

Overall, a cosmological GW spectrum spanning many orders of magnitudes in frequency has the potential to constrain the parameter space of modified theories of gravity, especially if the modifications occur in the early universe such as the RD era.

Data availability. The source code used for the numerical solutions of this study, the Pencil Code, along with the additions included for the present study, is freely available [30]; see also ref. [72] for the numerical data. The calculations and the routines generating the plots are publicly available on GitHub[9] [32].

Acknowledgments

Support through the grant 2019-04234 from the Swedish Research Council (Vetenskapsrådet) is gratefully acknowledged. Nordita is sponsored by Nordforsk. A.R.P. acknowledges support by the French National Research Agency (ANR) project MMUniverse (ANR-19-CE31-0020), the Shota Rustaveli National Science Foundation (SRNSF) of Georgia (grant FR/18-1462), and the Swiss National Science Foundation (grant 182044). We acknowledge the allocation of computing resources provided by the Swedish National Allocations Committee at the Center for Parallel Computers at the Royal Institute of Technology in Stockholm, and by the Grand Equipement National de Calcul Intensif (GENCI) to the project "Opening new windows on Early Universe with multi-messenger astronomy" (A0110412058).

A Numerical scheme

Following refs. [31, 73], we implement a matrix solver for the modified GW equation. Equation (2.5) can be expressed as

$$h''_{ij} + \sigma h'_{ij} + \omega^2 h_{ij} = 0 \tag{A.1}$$

where

$$\sigma \equiv \alpha_{\rm M}\mathcal{H}\,,\ \omega^2 \equiv c_{\rm T}^2 k^2 - \alpha_{\rm M}\mathcal{H}^2 - \frac{a''}{a}. \tag{A.2}$$

Then, assuming a solution of the type $h_{ij} = e_{ij} A e^{\lambda\eta}$ gives the characteristic equation

$$\lambda^2 + \sigma\lambda + \omega^2 = 0. \tag{A.3}$$

The eigenvalues λ can be obtained as

$$\lambda_{1,2} = -\frac{1}{2}\Big(\sigma \mp \sqrt{\sigma^2 - 4\omega^2}\Big). \tag{A.4}$$

For $\delta\eta \ll 1$, we approximate the solution by assuming that $\lambda'_{1,2} \approx \lambda''_{1,2} \approx 0$ during the time interval within time steps of the numerical solver. Then, the solution for the strains in equation (A.1) takes the form

$$h_{ij}(\eta + \delta\eta) = \mathcal{C}_{ij} e^{\lambda_1 \delta\eta} + \mathcal{D}_{ij} e^{\lambda_2 \delta\eta}, \tag{A.5}$$

$$h'_{ij}(\eta + \delta\eta) = \mathcal{C}_{ij}\lambda_1 e^{\lambda_1 \delta\eta} + \mathcal{D}_{ij}\lambda_2 e^{\lambda_2 \delta\eta}, \tag{A.6}$$

[9] https://github.com/AlbertoRoper/GW_turbulence/tree/master/horndeski

where $\mathcal{C}_{ij}$ and $\mathcal{D}_{ij}$ are constant amplitude coefficients evaluated at η. Equivalently, in matrix form, the solution can be rewritten as

$$\begin{pmatrix} h \\ h' \end{pmatrix}_{ij}^{\eta+\delta\eta} = \begin{pmatrix} e^{\lambda_1\delta\eta} & e^{\lambda_2\delta\eta} \\ \lambda_1 e^{\lambda_1\delta\eta} & \lambda_2 e^{\lambda_2\delta\eta} \end{pmatrix} \begin{pmatrix} \mathcal{C} \\ \mathcal{D} \end{pmatrix}_{ij}. \tag{A.7}$$

Hence, the amplitude coefficients can be obtained as

$$\begin{pmatrix} \mathcal{C} \\ \mathcal{D} \end{pmatrix}_{ij} = \begin{pmatrix} e^{\lambda_1\delta\eta} & e^{\lambda_2\delta\eta} \\ \lambda_1 e^{\lambda_1\delta\eta} & \lambda_2 e^{\lambda_2\delta\eta} \end{pmatrix}^{-1} \begin{pmatrix} h \\ h' \end{pmatrix}_{ij}^{\eta+\delta\eta} \tag{A.8}$$

$$= \frac{1}{(\lambda_2-\lambda_1)e^{(\lambda_1+\lambda_2)\delta\eta}} \begin{pmatrix} \lambda_2 e^{\lambda_2\delta\eta} & -e^{\lambda_2\delta\eta} \\ -\lambda_1 e^{\lambda_1\delta\eta} & e^{\lambda_1\delta\eta} \end{pmatrix} \begin{pmatrix} h \\ h' \end{pmatrix}_{ij}^{\eta+\delta\eta}, \tag{A.9}$$

and, in the limit $\delta\eta \to 0$, we get

$$\lim_{\delta\eta\to 0} \begin{pmatrix} \mathcal{C} \\ \mathcal{D} \end{pmatrix}_{ij} = \frac{1}{\lambda_2-\lambda_1} \begin{pmatrix} \lambda_2 & -1 \\ -\lambda_1 & 1 \end{pmatrix} \begin{pmatrix} h \\ h' \end{pmatrix}_{ij}^{\eta}, \tag{A.10}$$

where we assume that $\mathcal{C}_{ij}$ and $\mathcal{D}_{ij}$ are time-independent within time steps. Therefore, the time evolution of the relevant quantities can be obtained via a matrix multiplication as

$$\begin{pmatrix} h \\ h' \end{pmatrix}_{ij}^{\eta+\delta\eta} = \mathcal{M} \begin{pmatrix} h \\ h' \end{pmatrix}_{ij}^{\eta}, \tag{A.11}$$

where

$$\mathcal{M} = \frac{1}{\lambda_1-\lambda_2} \begin{pmatrix} \lambda_1 e^{\lambda_2\delta\eta} - \lambda_2 e^{\lambda_1\delta\eta} & e^{\lambda_1\delta\eta} - e^{\lambda_2\delta\eta} \\ \lambda_1\lambda_2(e^{\lambda_2\delta\eta} - e^{\lambda_1\delta\eta}) & \lambda_1 e^{\lambda_1\delta\eta} - \lambda_2 e^{\lambda_2\delta\eta} \end{pmatrix}. \tag{A.12}$$

In the case of $\sigma = 0$ and $\omega^2 = k^2$, the eigenvalues become $\lambda_{1,2} = \pm ik$ and the evolution matrix reduces to

$$\mathcal{M} = \begin{pmatrix} \cos k\delta\eta & \sin k\delta\eta \\ -\sin k\delta\eta & \cos k\delta\eta \end{pmatrix}. \tag{A.13}$$

B Numerical accuracy

In this section, we study the numerical accuracy of the runs. The GW solver in the Pencil Code has been made accurate to second order in time in the presence of a source T_{ij} under GR. However, the GW equation under modified theories of gravity lead to an equation that can be approximated within small but finite time steps under the assumption that the coefficients are constant in time, leading to the numerical solver described in section A. This method is accurate up to first order in the duration of the time step. As the coefficient variations in time become smaller, the error is also smaller, but the accuracy of the solver is still of first order. This is demonstrated in figure 10, where we show on the left panel the relative errors in the GW energy during RD and MD, and on the right panel the error during ΛD. Recall that during RD and MD, we use increasing time steps, represented by $n_{\rm incr}$ here. During ΛD, we use linear time steps, with the interval shown as $\eta_{\rm incr}$ in figure 10.

We also test the accuracy of the spectra in figure 11, where we show the saturated final energy spectrum for run M0A. Different colors indicate the linear time intervals during ΛD and the black curve is the spectrum obtained by running M0A entirely with increasing time

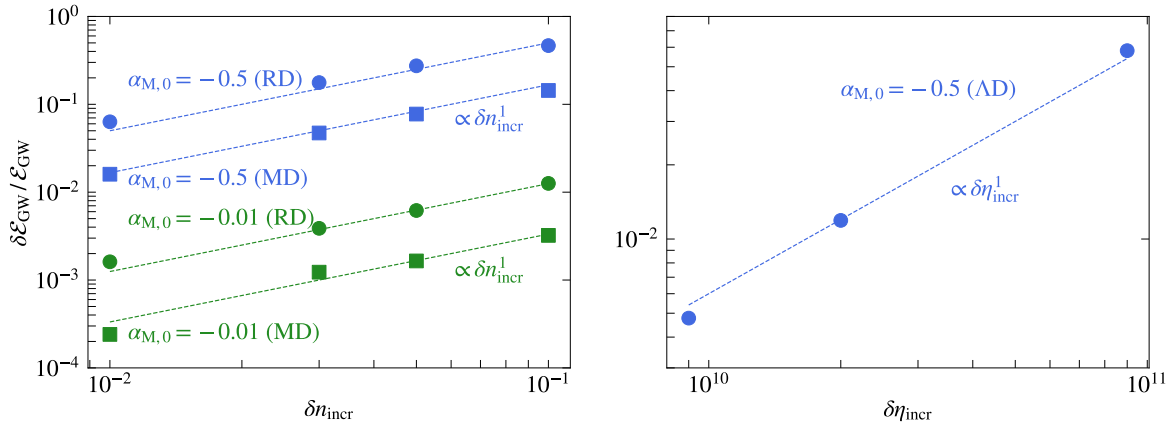

Figure 10: Relative errors as a function of the numerical time step. *Left panel*: Accuracy during RD (round dots) and MD (square dots) for $\alpha_{\rm M,0} = -0.5$ (blue) and $\alpha_{\rm M,0} = -0.01$ (green), where $\delta n_{\rm incr}$ indicates the difference in the time steps such that $\delta\eta = \eta\,\delta n_{\rm incr}$. *Right panel*: Accuracy during ΛD with $\delta\eta = \delta\eta_{\rm incr}$ directly indicating the linear time interval. The errors are calculated relative to the values obtained from using the smallest $\delta\eta_{\rm incr} = 5\times10^9$.

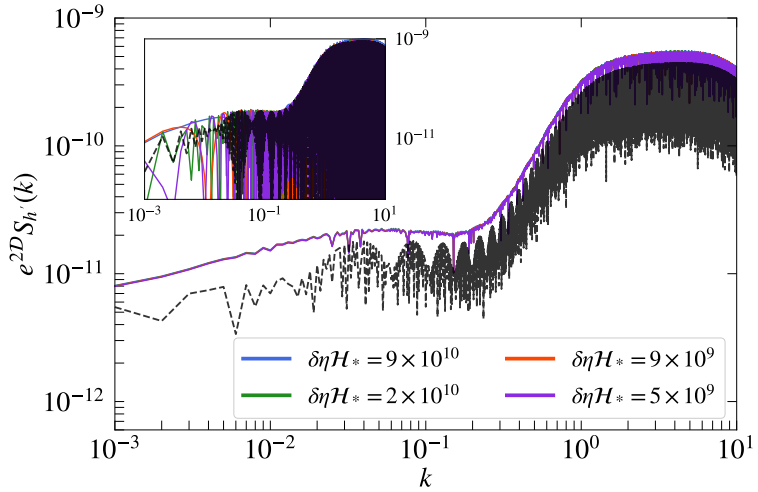

Figure 11: Saturated energy spectrum $e^{2\mathcal{D}}S_{h'}(k)$ for $\alpha_{\rm M,0} = -0.5$ (run M0A) with different time steps $\delta\eta\,\mathcal{H}_*$ during ΛD, where $n_{\rm incr} = 0.01$ is used during RD and MD. The black dashed curves correspond to the run M0A performed entirely, i.e., including ΛD, with increasing time steps with $n_{\rm incr} = 0.01$. The inset directly shows the spectrum at the final time without averaging over time oscillations.

steps using $n_{\rm incr} = 0.01$. In other words, the colored curves only differ from the black one from the linear time stepping during ΛD. We observe that all of the chosen values of $\delta\eta$ produce converging energy spectra after averaging over oscillations in time, although larger values of $\delta\eta$ result in more fluctuations in the numerical spectra (see the inset in figure 11). We also note that, compared to results from hybrid time steps, the entirely nonuniform time steps somewhat underestimate the final energy spectrum.

These accuracy tests justify our choice to use nonuniform time steps during RD and

MD to improve the efficiency of the simulations, and uniform linear time steps (with $\delta\eta$ that already gives converged results) during ΛD.

References

[1] A.G. Riess, S. Casertano, W. Yuan, L.M. Macri and D. Scolnic, *Large Magellanic Cloud Cepheid Standards Provide a 1% Foundation for the Determination of the Hubble Constant and Stronger Evidence for Physics beyond ΛCDM*, *Astrophys. J.* **876** (2019) 85 [1903.07603].

[2] A.G. Riess, S. Casertano, W. Yuan, J.B. Bowers, L. Macri, J.C. Zinn et al., *Cosmic Distances Calibrated to 1% Precision with Gaia EDR3 Parallaxes and Hubble Space Telescope Photometry of 75 Milky Way Cepheids Confirm Tension with ΛCDM*, *Astrophys. J. Lett.* **908** (2021) L6 [2012.08534].

[3] A.G. Riess et al., *A Comprehensive Measurement of the Local Value of the Hubble Constant with 1 km s^{-1} Mpc^{-1} Uncertainty from the Hubble Space Telescope and the SHOES Team*, *Astrophys. J. Lett.* **934** (2022) L7 [2112.04510].

[4] K.C. Wong et al., *H0LiCOW – XIII. A 2.4 per cent measurement of H0 from lensed quasars: 5.3σ tension between early- and late-Universe probes*, *Mon. Not. Roy. Astron. Soc.* **498** (2020) 1420 [1907.04869].

[5] D.W. Pesce et al., *The Megamaser Cosmology Project. XIII. Combined Hubble constant constraints*, *Astrophys. J. Lett.* **891** (2020) L1 [2001.09213].

[6] Planck collaboration, *Planck 2018 results. VI. Cosmological parameters*, *Astron. Astrophys.* **641** (2020) A6 [1807.06209].

[7] BOSS collaboration, *The clustering of galaxies in the completed SDSS-III Baryon Oscillation Spectroscopic Survey: cosmological analysis of the DR12 galaxy sample*, *Mon. Not. Roy. Astron. Soc.* **470** (2017) 2617 [1607.03155].

[8] L. Verde, T. Treu and A.G. Riess, *Tensions between the Early and the Late Universe*, *Nature Astron.* **3** (2019) 891 [1907.10625].

[9] S. Joudaki et al., *KiDS-450 + 2dFLenS: Cosmological parameter constraints from weak gravitational lensing tomography and overlapping redshift-space galaxy clustering*, *Mon. Not. Roy. Astron. Soc.* **474** (2018) 4894 [1707.06627].

[10] L. Perivolaropoulos and F. Skara, *Challenges for ΛCDM: An update*, *New Astron. Rev.* **95** (2022) 101659 [2105.05208].

[11] D. Lovelock, *The Einstein tensor and its generalizations*, *J. Math. Phys.* **12** (1971) 498.

[12] D. Lovelock, *The four-dimensionality of space and the einstein tensor*, *J. Math. Phys.* **13** (1972) 874.

[13] T. Clifton, P.G. Ferreira, A. Padilla and C. Skordis, *Modified Gravity and Cosmology*, *Phys. Rept.* **513** (2012) 1 [1106.2476].

[14] G.W. Horndeski, *Second-order scalar-tensor field equations in a four-dimensional space*, *Int. J. Theor. Phys.* **10** (1974) 363.

[15] C. Deffayet, X. Gao, D.A. Steer and G. Zahariade, *From k-essence to generalised Galileons*, *Phys. Rev. D* **84** (2011) 064039 [1103.3260].

[16] T. Kobayashi, M. Yamaguchi and J. Yokoyama, *Generalized G-inflation: Inflation with the most general second-order field equations*, *Prog. Theor. Phys.* **126** (2011) 511 [1105.5723].

[17] C. Brans and R.H. Dicke, *Mach's principle and a relativistic theory of gravitation*, *Phys. Rev.* **124** (1961) 925.

[18] B. Ratra and P.J.E. Peebles, *Cosmological Consequences of a Rolling Homogeneous Scalar Field*, *Phys. Rev. D* **37** (1988) 3406.

[19] A. De Felice and S. Tsujikawa, *f(R) theories*, *Living Rev. Rel.* **13** (2010) 3 [1002.4928].

[20] S.M. Carroll, A. De Felice, V. Duvvuri, D.A. Easson, M. Trodden and M.S. Turner, *The Cosmology of generalized modified gravity models*, *Phys. Rev. D* **71** (2005) 063513 [astro-ph/0410031].

[21] C. Armendariz-Picon, V.F. Mukhanov and P.J. Steinhardt, *Essentials of k essence*, *Phys. Rev. D* **63** (2001) 103510 [astro-ph/0006373].

[22] C. Deffayet, O. Pujolas, I. Sawicki and A. Vikman, *Imperfect Dark Energy from Kinetic Gravity Braiding*, *JCAP* **10** (2010) 026 [1008.0048].

[23] A. Nicolis, R. Rattazzi and E. Trincherini, *The Galileon as a local modification of gravity*, *Phys. Rev. D* **79** (2009) 064036 [0811.2197].

[24] M. Petronikolou, S. Basilakos and E.N. Saridakis, *Alleviating H_0 tension in Horndeski gravity*, 2110.01338.

[25] LIGO Scientific, Virgo, Fermi-GBM, INTEGRAL collaboration, *Gravitational Waves and Gamma-rays from a Binary Neutron Star Merger: GW170817 and GRB 170817A*, *Astrophys. J. Lett.* **848** (2017) L13 [1710.05834].

[26] J.M. Ezquiaga and M. Zumalacárregui, *Dark Energy After GW170817: Dead Ends and the Road Ahead*, *Phys. Rev. Lett.* **119** (2017) 251304 [1710.05901].

[27] C. de Rham and S. Melville, *Gravitational Rainbows: LIGO and Dark Energy at its Cutoff*, *Phys. Rev. Lett.* **121** (2018) 221101 [1806.09417].

[28] L. Lombriser and A. Taylor, *Breaking a Dark Degeneracy with Gravitational Waves*, *JCAP* **03** (2016) 031 [1509.08458].

[29] S. Arai and A. Nishizawa, *Generalized framework for testing gravity with gravitational-wave propagation. II. Constraints on Horndeski theory*, *Phys. Rev. D* **97** (2018) 104038 [1711.03776].

[30] Pencil Code collaboration, *The Pencil Code, a modular MPI code for partial differential equations and particles: multipurpose and multiuser-maintained*, *J. Open Source Softw.* **6** (2021) 2807 [2009.08231].

[31] A. Roper Pol, A. Brandenburg, T. Kahniashvili, A. Kosowsky and S. Mandal, *The timestep constraint in solving the gravitational wave equations sourced by hydromagnetic turbulence*, *Geophys. Astrophys. Fluid Dynamics* **114** (2020) 130 [1807.05479].

[32] A. Roper Pol, *GitHub project "GW_turbulence", 10.5281/zenodo.6045844; GW_turbulence*, .

[33] H. Takeda, S. Morisaki and A. Nishizawa, *Search for scalar-tensor mixed polarization modes of gravitational waves*, *Phys. Rev. D* **105** (2022) 084019 [2105.00253].

[34] C. Caprini, D.G. Figueroa, R. Flauger, G. Nardini, M. Peloso, M. Pieroni et al., *Reconstructing the spectral shape of a stochastic gravitational wave background with LISA*, *JCAP* **11** (2019) 017 [1906.09244].

[35] E. Bellini and I. Sawicki, *Maximal freedom at minimum cost: linear large-scale structure in general modifications of gravity*, *JCAP* **07** (2014) 050 [1404.3713].

[36] R.C. Nunes, M.E.S. Alves and J.C.N. de Araujo, *Primordial gravitational waves in Horndeski gravity*, *Phys. Rev. D* **99** (2019) 084022 [1811.12760].

[37] Y. He, A. Brandenburg and A. Sinha, *Tensor spectrum of turbulence-sourced gravitational waves as a constraint on graviton mass*, *JCAP* **07** (2021) 015 [2104.03192].

[38] A. Roper Pol, S. Mandal, A. Brandenburg, T. Kahniashvili and A. Kosowsky, *Numerical simulations of gravitational waves from early-universe turbulence*, *Phys. Rev. D* **102** (2020) 083512 [1903.08585].

[39] T. Kahniashvili, A. Brandenburg, G. Gogoberidze, S. Mandal and A. Roper Pol, *Circular polarization of gravitational waves from early-Universe helical turbulence*, *Phys. Rev. Res.* **3** (2021) 013193 [2011.05556].

[40] A. Brandenburg, G. Gogoberidze, T. Kahniashvili, S. Mandal, A. Roper Pol and N. Shenoy, *The scalar, vector, and tensor modes in gravitational wave turbulence simulations*, *Class. Quant. Grav.* **38** (2021) 145002 [2103.01140].

[41] A. Roper Pol, S. Mandal, A. Brandenburg and T. Kahniashvili, *Polarization of gravitational waves from helical MHD turbulent sources*, *JCAP* **04** (2022) 019 [2107.05356].

[42] A. Brandenburg, E. Clarke, Y. He and T. Kahniashvili, *Can we observe the QCD phase transition-generated gravitational waves through pulsar timing arrays?*, *Phys. Rev. D* **104** (2021) 043513 [2102.12428].

[43] A. Roper Pol, C. Caprini, A. Neronov and D. Semikoz, *Gravitational wave signal from primordial magnetic fields in the Pulsar Timing Array frequency band*, *Phys. Rev. D* **105** (2022) 123502 [2201.05630].

[44] R. Sharma and A. Brandenburg, *Low frequency tail of gravitational wave spectra from hydromagnetic turbulence*, *Phys. Rev. D* **106** (2022) 103536 [2206.00055].

[45] A. Brandenburg and R. Sharma, *Simulating Relic Gravitational Waves from Inflationary Magnetogenesis*, *Astrophys. J.* **920** (2021) 26 [2106.03857].

[46] A. Brandenburg, Y. He and R. Sharma, *Simulations of Helical Inflationary Magnetogenesis and Gravitational Waves*, *Astrophys. J.* **922** (2021) 192 [2107.12333].

[47] Y. He, A. Roper Pol and A. Brandenburg, *Leading-order nonlinear gravitational waves from reheating magnetogeneses*, 2110.14456.

[48] K. Saikawa and S. Shirai, *Primordial gravitational waves, precisely: The role of thermodynamics in the Standard Model*, *JCAP* **05** (2018) 035 [1803.01038].

[49] M.B. Hindmarsh, M. Lüben, J. Lumma and M. Pauly, *Phase transitions in the early universe*, *SciPost Phys. Lect. Notes* **24** (2021) 1 [2008.09136].

[50] A. Nishizawa, *Generalized framework for testing gravity with gravitational-wave propagation. I. Formulation*, *Phys. Rev. D* **97** (2018) 104037 [1710.04825].

[51] C. de Rham and S. Melville, *Gravitational Rainbows: LIGO and Dark Energy at its Cutoff*, *Phys. Rev. Lett.* **121** (2018) 221101 [1806.09417].

[52] T. Baker et al., *Measuring the propagation speed of gravitational waves with LISA*, 2203.00566.

[53] S.D. Odintsov, V.K. Oikonomou and R. Myrzakulov, *Spectrum of Primordial Gravitational Waves in Modified Gravities: A Short Overview*, *Symmetry* **14** (2022) 729 [2204.00876].

[54] J. Kennedy, L. Lombriser and A. Taylor, *Reconstructing Horndeski theories from phenomenological modified gravity and dark energy models on cosmological scales*, *Phys. Rev. D* **98** (2018) 044051 [1804.04582].

[55] J. Gleyzes, *Parametrizing modified gravity for cosmological surveys*, *Phys. Rev. D* **96** (2017) 063516 [1705.04714].

[56] M. Denissenya and E.V. Linder, *Gravity's Islands: Parametrizing Horndeski Stability*, *JCAP* **11** (2018) 010 [1808.00013].

[57] M. Yoshimura, *Stronger gravity in the early universe*, 2204.11384.

[58] M. Zumalacarregui, *Gravity in the Era of Equality: Towards solutions to the Hubble problem without fine-tuned initial conditions*, *Phys. Rev. D* **102** (2020) 023523 [2003.06396].

[59] M. Braglia, M. Ballardini, F. Finelli and K. Koyama, *Early modified gravity in light of the H_0 tension and LSS data*, *Phys. Rev. D* **103** (2021) 043528 [2011.12934].

[60] E.V. Linder, *Gravitational Wave Distances in Horndeski Cosmology*, 2108.11526.

[61] M.S. Turner, E.J. Weinberg and L.M. Widrow, *Bubble nucleation in first order inflation and other cosmological phase transitions*, *Phys. Rev. D* **46** (1992) 2384.

[62] NANOGrav collaboration, *The NANOGrav 12.5 yr Data Set: Search for an Isotropic Stochastic Gravitational-wave Background*, *Astrophys. J. Lett.* **905** (2020) L34 [2009.04496].

[63] B. Goncharov et al., *On the Evidence for a Common-spectrum Process in the Search for the Nanohertz Gravitational-wave Background with the Parkes Pulsar Timing Array*, *Astrophys. J. Lett.* **917** (2021) L19 [2107.12112].

[64] S. Chen et al., *Common-red-signal analysis with 24-yr high-precision timing of the European Pulsar Timing Array: inferences in the stochastic gravitational-wave background search*, *Mon. Not. Roy. Astron. Soc.* **508** (2021) 4970 [2110.13184].

[65] J. Antoniadis et al., *The International Pulsar Timing Array second data release: Search for an isotropic gravitational wave background*, *Mon. Not. Roy. Astron. Soc.* **510** (2022) 4873 [2201.03980].

[66] K. Schmitz, *New Sensitivity Curves for Gravitational-Wave Signals from Cosmological Phase Transitions*, *JHEP* **01** (2021) 097 [2002.04615].

[67] C.J. Moore, R.H. Cole and C.P.L. Berry, *Gravitational-wave sensitivity curves*, *Class. Quant. Grav.* **32** (2015) 015014 [1408.0740].

[68] N. Seto, S. Kawamura and T. Nakamura, *Possibility of direct measurement of the acceleration of the universe using 0.1-Hz band laser interferometer gravitational wave antenna in space*, *Phys. Rev. Lett.* **87** (2001) 221103 [astro-ph/0108011].

[69] J. Crowder and N.J. Cornish, *Beyond LISA: Exploring future gravitational wave missions*, *Phys. Rev. D* **72** (2005) 083005 [gr-qc/0506015].

[70] M. Punturo et al., *The Einstein Telescope: A third-generation gravitational wave observatory*, *Class. Quant. Grav.* **27** (2010) 194002.

[71] A. Neronov, A. Roper Pol, C. Caprini and D. Semikoz, *NANOGrav signal from magnetohydrodynamic turbulence at the QCD phase transition in the early Universe*, *Phys. Rev. D* **103** (2021) 041302 [2009.14174].

[72] Y. He, A. Roper Pol and A. Brandenburg, *Datasets of "Modified propagation of gravitational waves from the early radiation era", doi: 10.5281/zenodo.7408601 (v2022.12.07); see also* ***http://norlx65.nordita.org/~yutong/projects/Horndeski/*** *for easier access*, .

[73] A. Brandenburg and R. Sharma, *Simulating Relic Gravitational Waves from Inflationary Magnetogenesis*, *Astrophys. J.* **920** (2021) 26 [2106.03857].